

## A new microbial pathway for organophosphonate degradation catalyzed by two previously misannotated non-heme-iron oxygenases

Lauren Rajakovich, Maria-Eirini Pandelia, Andrew J Mitchell, Wei-chen Chang, Bo Zhang, Amie K. Boal, Carsten Krebs, and J. Martin Bollinger, Jr.

*Biochemistry*, **Just Accepted Manuscript** • DOI: 10.1021/acs.biochem.9b00044 • Publication Date (Web): 21 Feb 2019

Downloaded from <http://pubs.acs.org> on February 27, 2019

### Just Accepted

“Just Accepted” manuscripts have been peer-reviewed and accepted for publication. They are posted online prior to technical editing, formatting for publication and author proofing. The American Chemical Society provides “Just Accepted” as a service to the research community to expedite the dissemination of scientific material as soon as possible after acceptance. “Just Accepted” manuscripts appear in full in PDF format accompanied by an HTML abstract. “Just Accepted” manuscripts have been fully peer reviewed, but should not be considered the official version of record. They are citable by the Digital Object Identifier (DOI®). “Just Accepted” is an optional service offered to authors. Therefore, the “Just Accepted” Web site may not include all articles that will be published in the journal. After a manuscript is technically edited and formatted, it will be removed from the “Just Accepted” Web site and published as an ASAP article. Note that technical editing may introduce minor changes to the manuscript text and/or graphics which could affect content, and all legal disclaimers and ethical guidelines that apply to the journal pertain. ACS cannot be held responsible for errors or consequences arising from the use of information contained in these “Just Accepted” manuscripts.



1  
2  
3 A new microbial pathway for organophosphonate degradation catalyzed  
4  
5  
6 by two previously misannotated non-heme-iron oxygenases  
7  
8

9 **Funding.** This work was funded by the National Science Foundation (MCB-1330784 to J.M.B.  
10 and C.K.) and the National Institutes of Health (GM119707 to A.K.B, GM111978 to M.-E.P.,  
11 and GM127079 to C.K.). Use of the Advanced Photon Source, an Office of Science User Facility  
12 operated for the US Department of Energy (DOE) Office of Science by Argonne National  
13 Laboratory, was supported by the US DOE under Contract DE-AC02-06CH11357.  
14 GM/CA@APS has been funded in whole or in part with Federal funds from the National Cancer  
15 Institute (ACB-12002) and the National Institute of General Medical Sciences (AGM-12006).  
16 Use of the LS-CAT Sector 21 was supported by the Michigan Economic Development  
17 Corporation and Michigan Technology Tri-Corridor Grant 085P1000817.  
18  
19  
20  
21  
22

23 *Lauren J. Rajakovich<sup>†‡</sup>, Maria-Eirini Pandelia<sup>‡⊥</sup>, Andrew J. Mitchell<sup>†</sup>, Wei-chen Chang<sup>‡§</sup>, Bo*  
24 *Zhang<sup>‡¶</sup>, Amie K. Boal<sup>†‡\*</sup>, Carsten Krebs<sup>†‡\*</sup>, J. Martin Bollinger, Jr.<sup>†‡\*</sup>*  
25  
26  
27

28 <sup>†</sup>Department of Biochemistry and Molecular Biology and <sup>‡</sup>Department of Chemistry, The  
29 Pennsylvania State University, University Park, Pennsylvania 16802, United States  
30

31 <sup>#</sup>Present address: Department of Chemistry and Chemical Biology, Harvard University,  
32 Cambridge, Massachusetts 02138, United States  
33

34 <sup>⊥</sup>Present address: Department of Biochemistry, Brandeis University, Waltham, Massachusetts  
35 02453, United States  
36  
37

38 <sup>¶</sup>Present address: Whitehead Institute for Biomedical Research, Cambridge, Massachusetts 02142  
39

40 <sup>§</sup>Present address: Department of Chemistry, North Carolina State University, Raleigh, North  
41 Carolina 27695, United States  
42

43 <sup>¶</sup>Present address: REG Life Sciences, LLC, South San Francisco, California 94080  
44  
45

46 **\*Corresponding Authors**

47 akb20@psu.edu

48 cdk10@psu.edu

49 jmb21@psu.edu  
50  
51  
52  
53  
54  
55  
56  
57  
58  
59  
60

1  
2  
3 **Abbreviations:** Fe/2OG, iron(II)- and 2-oxoglutarate-dependent; MIOX, *myo*-inositol  
4 oxygenase; 2-AEP, 2-aminoethylphosphonate; (*R*)-OH-AEP, (*R*)-1-hydroxy-2-  
5 aminoethylphosphonate; BBOX,  $\gamma$ -butyrobetaine hydroxylase;  $\gamma$ bb,  $\gamma$ -butyrobetaine; *Lc*,  
6 *Leisingera caerulea*; TMAEP, 2-(trimethylammonio)ethylphosphonate; (*R*)-OH-TMAEP, (*R*)-1-  
7 hydroxy-2-(trimethylammonio)ethylphosphonate; *Ps*, *Pseudomonas sp. AK-1*; *Hs*, *Homo*  
8 *sapiens*; PC, phosphocholine; GABA,  $\gamma$ -aminobutyric acid;  $\gamma$ bb-3, 3-  
9 (trimethylammonio)propionic acid; TMLH,  $\epsilon$ -trimethyllysine hydroxylase; DMAEP, 2-  
10 (dimethylamino)ethylphosphonate; HD-MVDO, HD-domain mixed-valent diiron oxygenase

11  
12  
13  
14  
15  
16  
17  
18  
19  
20  
21 **Key Words:** gene annotation; enzyme; organophosphonate; iron oxygenase; HD-domain  
22  
23  
24  
25  
26  
27  
28  
29  
30  
31  
32  
33  
34  
35  
36  
37  
38  
39  
40  
41  
42  
43  
44  
45  
46  
47  
48  
49  
50  
51  
52  
53  
54  
55  
56  
57  
58  
59  
60

**ABSTRACT**

The assignment of biochemical functions to hypothetical proteins is challenged by functional diversification within many protein structural superfamilies. This diversification, which is particularly common for metalloenzymes, renders functional annotations that are founded solely on sequence and domain similarities unreliable and often erroneous. Definitive biochemical characterization to delineate functional sub-groups within these superfamilies will aid in improving bioinformatic approaches for functional annotation. We describe here the structural and functional characterization of two non-heme-iron oxygenases, TmpA and TmpB, which are encoded by a genomically clustered pair of genes found in more than 350 species of bacteria. TmpA and TmpB are functional homologues of a pair of enzymes (PhnY and PhnZ) that degrade 2-aminoethylphosphonate but instead act on its naturally occurring, quaternary ammonium analogue, 2-(trimethylammonio)ethylphosphonate (TMAEP). TmpA, an iron(II)- and 2-(oxo)glutarate-dependent oxygenase misannotated as a  $\gamma$ -butyrobetaine ( $\gamma$ bb) hydroxylase, shows no activity toward  $\gamma$ bb but efficiently hydroxylates TMAEP. The product, (*R*)-1-hydroxy-2-(trimethylammonio)ethylphosphonate [(*R*)-OH-TMAEP], then serves as the substrate for the second enzyme, TmpB. By contrast to its purported phosphohydrolytic activity, TmpB is an HD-domain oxygenase that uses a mixed-valent diiron cofactor to enact oxidative cleavage of the C–P bond of its substrate, yielding glycine betaine and phosphate. The high specificities of TmpA and TmpB for their *N*-trimethylated substrates suggests that they have evolved specifically to degrade TMAEP, which was not previously known to be subject to microbial catabolism. This study thus adds to the growing list of known pathways through which microbes break down organophosphonates to harvest phosphorus, carbon, and nitrogen in nutrient-limited niches.

## INTRODUCTION

Members of a given metalloenzyme superfamily share a conserved protein architecture and characteristic type of metallocofactor. Even with conservation of both protein and cofactor structures, superfamily members can promote fundamentally different reaction types, transform structurally dissimilar substrates, or both.<sup>1-4</sup> This functional diversification limits the utility of domain conservation and sequence similarity for *de novo* prediction of metalloenzyme activity.<sup>5-7</sup> This problem is not unique to metalloenzymes; an estimated 98% of all gene ontology annotations are algorithmically generated and not subsequently curated,<sup>8-10</sup> leading to misannotations that are propagated and amplified as the number of fully sequenced genomes rapidly grows. However, given the established roles of metalloenzymes in central life processes, misannotation of these proteins, in particular, could be hindering discovery of novel functions with important biomedical or environmental implications.

Functional diversification of a single metalloprotein superfamily is exemplified by the iron(II)- and 2-(oxo)glutarate-dependent (Fe/2OG) oxygenases,<sup>2</sup> with ~ 100,000 members classified by the InterPro database (IPR005123, v.71.0). Fe/2OG oxygenases share a  $\beta$ -sandwich, cupin structural fold<sup>11</sup> and a largely conserved sequence motif, **HxD/EX(40-160)H**, that contributes the protein ligands coordinating the characteristic mononuclear non-heme Fe(II) cofactor.<sup>12,13</sup> Fe/2OG enzymes couple reduction of dioxygen to the oxidative decarboxylation of 2OG to succinate and CO<sub>2</sub>. This reaction generates an Fe(IV)-oxo (ferryl) intermediate,<sup>14</sup> which, in most cases, extracts two electrons from the primary substrate to balance the complete four-electron reduction of O<sub>2</sub>. Whereas hydroxylation is the most common outcome, halogenation, desaturation, and cyclization reactions also occur according to the same functional logic and within this single, conserved protein architecture.<sup>15</sup> Prediction of the reaction that a newly

1  
2  
3 discovered member will catalyze is further complicated by the broad substrate scope of the  
4 superfamily, which varies from simple small molecules to complex natural products to even  
5 large macromolecules, including proteins and nucleic acids. Even high-resolution structures  
6 generally do not reveal the substrate of a given Fe/2OG oxygenase, owing to the conformational  
7 disorder of substrate-interacting loop regions often seen in the absence of the primary substrate.<sup>11</sup>  
8  
9

10  
11  
12  
13  
14 HD-domain proteins comprise another large and sparsely characterized superfamily of  
15 metalloenzymes,<sup>4</sup> with ~ 160,000 members in the InterPro database (IPR006674, v.71.0). The  
16 namesake domain of the superfamily has a characteristic **H<sub>x</sub><sub>a</sub>HD<sub>x</sub><sub>b</sub>D** sequence motif, which  
17 contributes the ligands for a single divalent metal ion. At the time this superfamily was first  
18 recognized, all members with known functions were hydrolases acting on phosphate esters or  
19 anhydrides,<sup>16-19</sup> leading to the automatic annotation of members discovered subsequently as  
20 putative phosphohydrolases.<sup>4</sup> However, more recent biochemical studies on several HD-domain  
21 proteins have expanded the range of known metal cofactor types and catalytic activities  
22 associated with the superfamily. Most notably, two HD-domain proteins – *myo*-inositol  
23 oxygenase (MIOX) and (*R*)-1-hydroxy-2-aminoethylphosphonate oxygenase (PhnZ) – were  
24 shown to activate dioxygen for carbon-carbon and carbon-phosphorus bond-cleavage reactions,  
25 respectively.<sup>20-22</sup> These enzymes harbor histidine- and carboxylate-coordinated diiron cofactors,  
26 which function in the mixed-valent Fe<sub>2</sub>(II/III) oxidation state to activate the primary substrate  
27 and dioxygen for four-electron oxidation reactions.<sup>20,21,23</sup> The capacity of an HD-domain protein  
28 to bind *two* metals in the active site can be inferred from the observation of two additional,  
29 conserved histidine residues (which serve as metal ligands) in the primary structure between the  
30 aspartate residues of the canonical domain (H<sub>x</sub><sub>a</sub>HD<sub>x</sub><sub>b</sub>H<sub>x</sub><sub>c</sub>H<sub>x</sub><sub>d</sub>D).<sup>21,24,25</sup> The dinuclear nature of  
31 the metal cofactor in a given HD-domain protein can thus be predicted from sequence, but this  
32  
33  
34  
35  
36  
37  
38  
39  
40  
41  
42  
43  
44  
45  
46  
47  
48  
49  
50  
51  
52  
53  
54  
55  
56  
57  
58  
59  
60

1  
2  
3 recognition is of limited value in assigning a specific activity, because a subset of proteins  
4 harboring dinuclear cofactors use them to promote the type of hydrolytic reaction for which the  
5 enzyme family was initially known.<sup>26-28</sup> In other words, the metal nuclearity of the cofactor does  
6 not, by itself, serve to distinguish the two major functional subclasses, phosphohydrolases and  
7 oxygenases. These recent discoveries of diversity in both cofactor structure and catalytic activity  
8 invalidate the still persistent practice of automatic annotation of newly discovered HD-domain  
9 proteins as phosphohydrolases.

10  
11  
12  
13  
14  
15  
16  
17  
18  
19 The functional diversity within structural superfamilies, exemplified by these two cases,  
20 necessitates additional experimental and bioinformatic evaluation to supplement sequence- and  
21 domain-based annotations in order to improve functional predictions (of both the substrate and  
22 reaction type) for hypothetical metalloenzymes.<sup>29-32</sup> In bacteria, genomic context can be a  
23 valuable tool for deducing the identities of enzyme substrates and/or products.<sup>33-36</sup> The enzymes  
24 of a given metabolic pathway are frequently encoded by genes in a single operon or cluster,<sup>37</sup>  
25 allowing one to infer that the product of one enzyme will serve as the substrate for another when  
26 the corresponding genes have such synteny. A relevant example is the recently discovered  
27 pathway for degradation of the most abundant environmental organophosphonate compound, 2-  
28 aminoethylphosphonate (2-AEP). Two syntenic genes encode the enzymes PhnY and PhnZ,  
29 which enable many marine bacteria to catabolize this compound.<sup>22</sup> PhnY is an Fe/2OG  
30 oxygenase that hydroxylates C1 of 2-AEP to generate (*R*)-1-hydroxy-2-aminoethylphosphonate  
31 [(*R*)-OH-AEP].<sup>22</sup> This product serves as the substrate for PhnZ, an HD-domain diiron oxygenase,  
32 which cleaves the C–P bond to yield the final degradation products, phosphate and glycine.<sup>21,22,24</sup>

33  
34  
35  
36  
37  
38  
39  
40  
41  
42  
43  
44  
45  
46  
47  
48  
49  
50  
51  
52 In this work, we identified a similar two-gene operon that encodes an Fe/2OG oxygenase  
53 and an HD-domain protein in the genomes of > 350 bacteria. In almost all cases, the Fe/2OG  
54  
55  
56  
57

1  
2  
3 oxygenase, which we herein designate TmpA, had been annotated as a  $\gamma$ -butyrobetaine  
4 hydroxylase (BBOX). BBOXs catalyze hydroxylation of C3 of  $\gamma$ -butyrobetaine ( $\gamma$ bb) to yield L-  
5 carnitine in the last step of its biosynthesis in eukaryotes<sup>38</sup> and in the first step of bacterial  $\gamma$ bb  
6 degradation for carbon and nitrogen assimilation.<sup>39,40</sup> The HD-domain protein, herein designated  
7 TmpB, was largely annotated as a phosphohydrolase. However, the moderate sequence similarity  
8 of TmpB to the HD-domain oxygenase PhnZ (~ 30% identity), including conservation of the  
9 extended **H<sub>X<sub>a</sub></sub>****HD<sub>X<sub>b</sub></sub>****H<sub>X<sub>c</sub></sub>****H<sub>X<sub>d</sub></sub>****D** dimetal sequence motif, and its analogous genomic synteny with an  
10 Fe/2OG oxygenase led us to suspect that TmpB might actually be a new HD-domain mixed-  
11 valent diiron oxygenase (HD-MVDO). By biochemical and structural analyses, we reassigned  
12 the functions of this pair of proteins encoded in the genome of the marine bacterium *Leisingera*  
13 *caerulea* (*Lc*).<sup>41,42</sup> TmpA and TmpB catalyze the two steps of a previously unidentified pathway  
14 for degradation of the naturally occurring organophosphonate 2-  
15 (trimethylammonio)ethylphosphonate (TMAEP). TmpA hydroxylates TMAEP at C1, thereby  
16 providing the substrate for TmpB, which promotes the O<sub>2</sub>-dependent oxidative cleavage of the  
17 C–P bond to yield glycine betaine and phosphate. Biochemical and spectroscopic evidence  
18 demonstrate that TmpA and TmpB are highly specific for their *N*-trimethylated substrates and  
19 are thus unlikely to overlap functionally with the PhnY/Z pair that degrades the corresponding  
20 unmethylated compound. The X-ray crystal structures of TmpA and TmpB rationalize this  
21 selectivity, while also confirming their similarities to BBOX and PhnZ, respectively, which was  
22 anticipated from sequence similarity and led to their initial misannotation. The biochemical and  
23 structural characterization of these enzymes, together with their genomic context, can inform  
24 functional predictions for other uncharacterized Fe/2OG and HD-domain enzymes.  
25  
26  
27  
28  
29  
30  
31  
32  
33  
34  
35  
36  
37  
38  
39  
40  
41  
42  
43  
44  
45  
46  
47  
48  
49  
50  
51  
52  
53  
54  
55  
56  
57  
58  
59  
60



## EXPERIMENTAL PROCEDURES

**Materials.** All chemicals used for protein over-expression and purification were purchased from Sigma-Aldrich (St. Louis, USA), unless stated otherwise.

**Preparation of *Lc TmpA*, *Lc TmpB*, and *Ps BBOX*.** Detailed procedures for over-expression and purification of the proteins are provided in the Supporting Information.

**Preparation of *PhnY* and *PhnZ*.** Proteins were prepared as previously described.<sup>21</sup>

**Construction of Sequence Similarity Networks.** We generated the sequence similarity network (SSN) using the Enzyme Function Initiative – Enzyme Similarity Tool (EFI-EST) web-based server<sup>43</sup> and visualized it in Cytoscape (v 3.2.1).<sup>44</sup> We constructed a network of all sequences either (1) classified with the IPR003819 (v 59.0) “TauD/TfdA-like” domain and a length of > 350 amino acids or (2) having an *E*-value threshold  $< 1 \times 10^{-10}$  in a Basic Local Alignment Search Tool (BLAST) query of the National Center for Biotechnology Information (NCBI) and the Joint Genome Institute – Integrated Microbial Genomes (JGI-IMG)<sup>45</sup> databases with the *Lc TmpA* sequence. Sequences with > 90% identity were binned into single nodes, and an initial pairwise alignment score threshold of  $< 1 \times 10^{-50}$  was selected for vertices (Figure S1). Further network analysis was performed by increasing the threshold stringency, as described in the Supporting Information (Figures S2 and S3; Figure 2).

**Synthesis of DMAEP and TMAEP.** Procedures used to synthesize 2-(dimethylamino)-ethylphosphonate (DMAEP) and 2-(trimethylammonio)ethylphosphonate (TMAEP) and characterization of the synthetic compounds are provided in the Supporting Information.

**Enzymatic production of (*R*)-1-hydroxy-2-(trimethylammonio)ethylphosphonate [(*R*)-OH-TMAEP].** The (*R*)-OH-TMAEP substrate for *TmpB* was prepared from TMAEP by enzymatic

1  
2  
3 conversion catalyzed by TmpA. A reaction (0.1 L) containing 0.005 mM TmpA, 0.01 mM  
4  $(\text{NH}_4)_2\text{Fe}(\text{SO}_4)_2$ , 3 mM 2OG and 3 mM TMAEP was prepared in 25 mM ammonium acetate  
5  
6 buffer (pH 7.5) and was incubated at room temperature with constant stirring and flushing with  
7  
8 air. The product was purified according to the procedure used for preparation of (*R*)-OH-AEP<sup>21</sup>  
9  
10 and was analyzed by NMR (Figure S4): <sup>13</sup>C NMR ( $\text{D}_2\text{O}$ )  $\delta = 68.83$  (d,  $J = 12.5$  Hz), 64.76 (d,  $J =$   
11  
12 145.0), and 62.39 ppm; <sup>31</sup>P NMR ( $\text{D}_2\text{O}$ )  $\delta = 13.0$  ppm; <sup>1</sup>H NMR ( $\text{D}_2\text{O}$ )  $\delta = 3.60$  (m, 1H), 3.45  
13  
14 (m, 1H), and 3.37 (m, 1H), 1.74 (s, 9H). The stereochemistry was determined from the x-ray  
15  
16 crystal structures of the TmpA product and TmpB substrate complexes.  
17  
18  
19

20  
21 **Multiple-turnover enzyme assays.** End-point reactions to test for activity of Fe/2OG  
22  
23 oxygenases with substrates and analogues contained final concentrations of 0.02 mM *apo*-TmpA  
24  
25 (or *apo*-BBOX or *apo*-PhnY), 0.03 mM  $(\text{NH}_4)_2\text{Fe}(\text{SO}_4)_2$ , 0.4 mM sodium L-ascorbate, 3 mM  
26  
27 2OG, 2 mM substrate and 0.2 mM 2,2,3,3-<sup>2</sup>H<sub>4</sub>-succinate (*d*<sub>4</sub>-succinate) in 50 mM sodium 2-[4-  
28  
29 (2-hydroxyethyl)-piperazin-1-yl] ethanesulfonate (HEPES) buffer, pH 7.5. End-point reactions to  
30  
31 test for activity of HD-domain proteins with substrates and analogues contained final  
32  
33 concentrations of 0.01 mM aerobically-isolated TmpB (or aerobically-isolated PhnZ), 0.5 mM  
34  
35 sodium L-ascorbate and 2 mM substrate in 50 mM sodium HEPES, pH 7.5. All reaction  
36  
37 components ( $\text{O}_2$ -free) were mixed in an anoxic chamber and brought to 0.10 mL by addition of  
38  
39  $\text{O}_2$ -free buffer. The solutions were then removed from the chamber and the reactions were  
40  
41 initiated by addition of 0.90 mL cold, air-saturated buffer ( $\sim 0.4$  mM  $\text{O}_2$  at 5 °C). Reactions were  
42  
43 incubated on ice ( $\sim 3$  °C), stirred, and flushed with air for 4 h. Aliquots for LC-MS analysis (0.1  
44  
45 mL) were treated with 0.005 mL formic acid (5% final), and aliquots for <sup>31</sup>P-NMR analysis (0.48  
46  
47 mL) were treated with 0.02 mL acetic acid (4% final), to terminate the reactions. Minor  
48  
49 deviations from these general procedures are described in the appropriate figure legends.  
50  
51  
52  
53  
54  
55  
56  
57  
58  
59  
60

1  
2  
3 **Determination of TmpA coupling ratio.** Reaction solutions (0.1 mL) containing 0.22 mM *apo-*  
4 TmpA, 0.2 mM  $(\text{NH}_4)_2\text{Fe}(\text{SO}_4)_2$ , 0.4 mM TMAEP, 0.1 mM *d*<sub>4</sub>-succinate and varying  
5 concentrations of 2OG (0, 0.02, 0.04, 0.06, 0.08, 0.1, 0.12, 0.14, or 0.16 mM) in 50 mM sodium  
6 HEPES, pH 7.5, were prepared in an anoxic chamber. Assay solutions were removed from the  
7 anoxic chamber and mixed with an equal volume of O<sub>2</sub>-saturated sodium HEPES buffer, pH 7.5  
8 (~1.8 mM O<sub>2</sub> at 5 °C). Reactions were quenched after 10 min by addition of 0.01 mL formic acid  
9 and were clarified by passage through centrifugal filter devices with 10 kDa molecular weight  
10 cut-off (Pall Corporation, Westborough, MA). Succinate and TMAEP were quantified by the  
11 LC-MS analysis described below.  
12  
13  
14  
15  
16  
17  
18  
19  
20  
21  
22

23 **<sup>31</sup>P-NMR sample preparation and spectroscopy.** For <sup>31</sup>P-NMR measurements, sodium  
24 dithionite, ethylenediaminetetraacetic acid (EDTA), and D<sub>2</sub>O were added to the samples to final  
25 concentrations of 0.2 mM, 0.2 mM, and 20 % (v/v), respectively. Solution <sup>31</sup>P-NMR spectra of  
26 the various phosphorus-containing compounds were recorded at room temperature on an AVX-  
27 360 or HD-500 Bruker spectrometer. The spectra were recorded with a 1D sequence with power-  
28 gated <sup>1</sup>H decoupling. Chemical shifts are quoted with respect to a phosphoric acid solution (0  
29 ppm) prepared in the reaction buffer (sodium HEPES buffer, pH 7.5 with acetic acid, EDTA,  
30 sodium dithionite in D<sub>2</sub>O). NMR spectra were further processed with the freely available  
31 Spinworks (version 1.3.8.1) software (Dr. Kirk Marat, University of Manitoba, Canada).  
32  
33  
34  
35  
36  
37  
38  
39  
40  
41  
42  
43

44 **High performance liquid chromatography – mass spectrometry (LC-MS).** LC-MS analysis  
45 was carried out on an Agilent 1200 series LC system coupled to a triple quadrupole mass  
46 spectrometer (Agilent 6410 QQQ LC/MS; Agilent Technologies, Santa Clara, CA). Succinate  
47 was detected by injection of a 2-μL aliquot of a filtered sample (0.2 μm filter) onto an extend-  
48 C18 Agilent column equilibrated in 99% solvent A (water with 0.1% formic acid) and 1%  
49  
50  
51  
52  
53  
54  
55  
56  
57  
58  
59  
60

1  
2  
3 solvent B (acetonitrile). Succinate was eluted from the column with an isocratic mobile phase of  
4  
5 99% solvent A and 1% solvent B at a flow rate of 0.4 mL/min for 10 min. Detection of succinate  
6  
7 and the internal standard  $d_4$ -succinate was performed by electrospray ionization mass  
8  
9 spectrometry (ESI-MS) (source parameters: gas temperature = 350 °C, gas flow = 9 L/min,  
10  
11 nebulizer pressure = 40 psi, capillary voltage = 4000 V) in the negative mode with single ion  
12  
13 monitoring at mass-to-charge ratios ( $m/z$ ) of 117 and 121, respectively (fragmentor voltage = 135  
14  
15 V, dwell time = 200 s, delta EMV = 200 V). Succinate was quantified by multiplying the known  
16  
17 concentration of  $d_4$ -succinate by the ratio of the integrated peak areas for succinate and  $d_4$ -  
18  
19 succinate.  
20  
21  
22  
23

24 For analysis of quaternary ammonium compounds, samples (2  $\mu$ L) were injected onto a  
25  
26 SeQuant ZIC-HILIC (3.5  $\mu$ m, 100 Å, PEEK 150 x 2.1 mm) column (Merck, Darmstadt,  
27  
28 Germany) equilibrated in 2% solvent A (10 mM ammonium acetate with 0.2% formic acid) and  
29  
30 98% solvent B (acetonitrile). The reaction mixture was separated with a flow rate of 0.3 mL/min  
31  
32 by applying a linear gradient of 2% - 75% solvent A over 28 min then returning to 2% solvent A  
33  
34 over 25 min and washing with 2% solvent A for 7 min before the next injection. The compounds  
35  
36 were detected by ESI-MS (source parameters: gas temperature = 350 °C, gas flow = 9 L/min,  
37  
38 nebulizer pressure = 40 psi, capillary voltage = 4000 V) in the positive mode with single ion  
39  
40 monitoring (fragmentor voltage = 135 V, dwell time = 200 s, delta EMV = 200 V) at  $m/z$  ratios  
41  
42 provided in Table S1. Metabolites were quantified by comparison of integrated peak intensities  
43  
44 to that of an internal standard ( $\gamma$ bb or  $\gamma$ bb-3) of known concentration.  
45  
46  
47  
48

49 For analysis of primary amine compounds, samples (2  $\mu$ L) were injected onto a SeQuant  
50  
51 ZIC-HILIC (3.5  $\mu$ m, 100 Å, PEEK 150 x 2.1 mm) column (Merck, Darmstadt, Germany)  
52  
53 equilibrated in 5% solvent A (water with 0.1% formic acid) and 95% solvent B (acetonitrile with  
54  
55  
56  
57

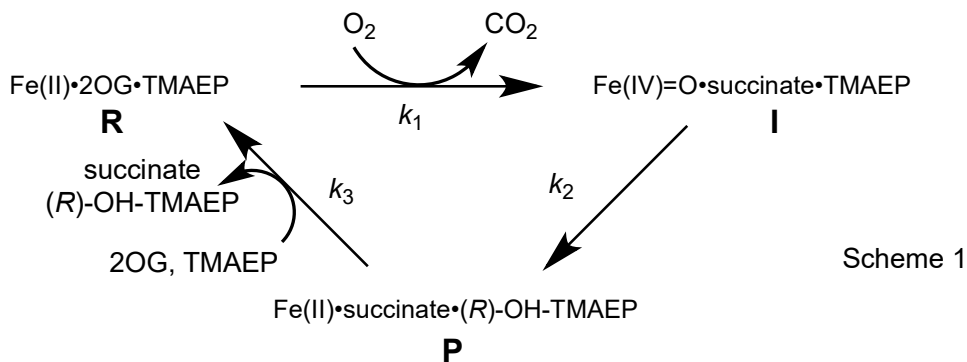
0.1% formic acid). The reaction mixture was separated with a flow rate of 0.3 mL/min by applying a linear gradient of 5% - 70% solvent A over 25 min, then returning to 5% solvent A over 25 min and washing with 5% solvent A for 10 min before the next injection. The compounds were detected by ESI-MS (source parameters: gas temperature = 350 °C, gas flow = 9 L/min, nebulizer pressure = 40 psi, capillary voltage = 4000 V) in the positive mode with single ion monitoring (fragmentor voltage = 135 V, dwell time = 200 s, delta EMV = 200 V) at  $m/z$  values listed in Table S2. Quantification was as described above, with  $^{13}\text{C}$ -glycine used as the internal standard.

**Stopped-flow absorption (SF-Abs) measurements and data analysis.** SF-Abs experiments were carried out at 5 °C with an Applied Photophysics Ltd. (Leatherhead, UK) SX20 stopped-flow spectrophotometer housed in an anoxic chamber (Labmaster, MBraun, Stratham, USA). The instrument was configured for single-mixing, an optical pathlength of 1 cm, and data acquisition with polychromatic light and a photodiode-array (PDA) detector. Time-dependent absorption spectra (1,000 points) were acquired with a logarithmic time base. Specific reaction conditions are provided in the appropriate figure legends.

Absorbance-versus-time traces were analyzed according to equation 1, which relates to the cycle of three consecutive, first-order, irreversible reactions shown in Scheme 1. Note that, under the conditions of the experiments (limiting  $\text{O}_2$  and excess 2OG and TMAEP), the  $\text{TmpA}\cdot\text{Fe(II)}\cdot 2\text{OG}\cdot\text{TMAEP}$  reactant complex (**R**) re-forms at completion. Although the initial step (**R**  $\rightarrow$  **I**) requires  $\text{O}_2$  and is expected to be kinetically first order in this reactant, the excess of the enzyme reactant is sufficient to make the approximation of pseudo-first-order kinetics in this step an acceptably good one. Similarly, the rate of the **P**  $\rightarrow$  **R** step may depend on the substrate concentrations, but both are present in large (pseudo-first-order) excess. Moreover,

conversion of the product complex to the reactant complex may, as in other Fe/2OG systems, also be rate-limited by product dissociation.<sup>46</sup> Absorbance was monitored as a function of time at 519 nm, where **R** absorbs maximally, the TmpA•Fe(IV)=O•succinate•TMAEP intermediate state (**I**) is nearly isobestic with **R**, and the TmpA•Fe(II)•succinate•(R)-OH-TMAEP complex (**P**) is transparent, and 320 nm, where **I** absorbs intensely and **R** and **P** absorb much less intensely. In the presentation and analysis of the traces, the final absorbance was set to zero by subtraction of a constant from all absorbance values. In addition, because the first step is quite fast and nearly unresolved,  $k_1$  was set in the regression analysis to a value of  $750 \text{ s}^{-1}$  (corresponding to a true second-order rate constant of  $\sim 1.5 \times 10^6 \text{ M}^{-1}\text{s}^{-1}$ ). This value represents a lower limit: values greater than  $750 \text{ s}^{-1}$  gave equally good fits, but lesser values gave noticeably poorer agreement.

$$\Delta A = [\text{R}]_0 \left\{ \left( \epsilon_1 - \epsilon_{\text{R}} \right) \frac{k_1}{k_2 - k_1} (e^{-k_1 t} - e^{-k_2 t}) + \left[ \epsilon_{\text{P}} - \epsilon_{\text{R}} \right] \frac{k_2 \cdot k_1}{k_2 - k_1} \left( \frac{1}{k_3 - k_1} (e^{-k_1 t} - e^{-k_3 t}) - \frac{1}{k_3 - k_2} (e^{-k_2 t} - e^{-k_3 t}) \right) \right\} \quad (1)$$



**Crystallization and x-ray structure solution of TmpA and TmpB.** For all structures, crystallographic datasets were collected at the GM/CA 21ID-F/G and LS-CAT 23ID-B beamlines of the Advanced Photon Source at Argonne National Lab, and the resulting diffraction images were processed with the software package HKL2000.<sup>47</sup> Refinement and model building were performed with the programs Refmac<sup>48</sup> and COOT,<sup>49</sup> respectively. A summary of data collection and refinement statistics for all structures can be found in Tables S1 and S2.

1  
2  
3 Ramachandran outlier analysis and other validation procedures were carried out using the  
4 Molprobity server.<sup>50</sup> Figures were generated in the PyMOL molecular graphics software package  
5  
6  
7  
8 (Schrödinger LLC).

9  
10 In an anoxic chamber at 25 °C, an O<sub>2</sub>-free solution containing TmpA (15 mg/mL), 0.35  
11 mM (NH<sub>4</sub>)<sub>2</sub>Fe(SO<sub>4</sub>)<sub>2</sub>, and 1.75 mM 2OG was mixed in a 2:1 (v:v) ratio with a precipitant  
12 solution containing of 1.0-1.4 M Li<sub>2</sub>SO<sub>4</sub> and 1.6-1.8 M (NH<sub>4</sub>)<sub>2</sub>SO<sub>4</sub> in hanging drop vapor  
13 diffusion trials. TMAEP was soaked into existing crystals by 1:1 (v:v) mixing of crystal drops  
14 with 20 mM TMAEP prepared in the precipitant solution followed by a 4-5-h incubation at 25  
15 °C. Crystals were prepared for data collection by cryoprotection in the precipitant solution  
16 supplemented with 19% (v/v) glycerol, mounting on rayon loops, and flash freezing in liquid  
17 nitrogen. The structure of the product complex of TmpA was obtained after adventitious  
18 exposure of crystals (described below) to O<sub>2</sub> during crystallization, likely due to incomplete  
19 removal of O<sub>2</sub> in the original screen. These crystals were obtained after mixing a solution of O<sub>2</sub>-  
20 free TmpA (15 mg/mL), 0.35 mM (NH<sub>4</sub>)<sub>2</sub>Fe(SO<sub>4</sub>)<sub>2</sub>, 1.75 mM 2OG and 1.75 mM TMAEP with  
21 an equal volume of a precipitant solution (from a commercial screen by Qiagen) consisting of 1.1  
22 M sodium malonate (pH 7.0), 0.1 M sodium HEPES (pH 7.0) and 0.5 % Jeffamine ED-2001 (pH  
23 7.0) in a sitting-drop diffusion trial in an anoxic chamber. Crystals were prepared for data  
24 collection via soaking in the well solution supplemented with 25% (v/v) glycerol as a  
25 cryoprotectant, mounting on rayon loops, and flash freezing in liquid nitrogen.

26  
27 The structure of TmpA with its phosphonate-containing product bound was solved by  
28 molecular replacement using the software package PHASER,<sup>51</sup> with a truncated *Hs* BBOX  
29 structure (PDB accession code 3O2G, residues 101-388) as the search model. The resulting  
30 electron density map was subjected to an autobuilding procedure using the software package  
31  
32  
33  
34  
35  
36  
37  
38  
39  
40  
41  
42  
43  
44  
45  
46

1  
2  
3 ARP/wARP,<sup>52</sup> followed by manual model building in Coot. All other TmpA structures were  
4 solved by molecular replacement using PHASER,<sup>51</sup> with the structure of the TmpA product  
5 complex as the search model. The TMAEP and (*R*)-OH-TMAEP ligands were generated using  
6 the software package JLigand.<sup>53</sup>  
7  
8  
9  
10

11  
12 The structure of the TmpA•Fe(II)•2OG complex contains residues 1-375 in chain A and  
13 residues 1-376 in chain B. The model for each chain additionally contains two residues at the N-  
14 terminus from the linker to the His<sub>6</sub> affinity tag. A single iron ion is modeled in chains A and B,  
15 but electron density for the 2OG co-substrate is observed only in chain A. The final model also  
16 contains 4 sulfate ions and 464 water molecules. The structure of the  
17 TmpA•Fe(II)•2OG•TMAEP complex consists of residues 1-376 in chain A, residues 1-188 and  
18 196-376 in chain B, 2 iron ions, 1 2OG molecule, 1 TMAEP molecule (ligand TMP), 1 sulfate  
19 ion, and 521 water molecules. The model for each chain contains two or three residues at the N-  
20 terminus from the His<sub>6</sub> affinity tag. The TMAEP and 2OG molecules are modeled only in chain  
21 A. A loop containing residues 189-195 is disordered in chain B, but is ordered in chain A. The  
22 structure of the TmpA•product complex contains residues 1-376 in both chains A and B, 2 iron  
23 ions, 1 (*R*)-OH-TMAEP molecule (TMO), and 483 water molecules. The model for each chain  
24 contains two residues at the N-terminus from the His<sub>6</sub> affinity tag. Electron density for the (*R*)-  
25 OH-TMAEP product is observed solely in chain A. The electron density in the co-product site of  
26 chain A likely reflects mixed occupancy by succinate, acetate, and water molecules (Figure S15)  
27 and was therefore left unmodeled.  
28  
29  
30  
31  
32  
33  
34  
35  
36  
37  
38  
39  
40  
41  
42  
43  
44  
45  
46  
47  
48

49 In an anoxic chamber, an O<sub>2</sub>-free solution of TmpB (10 mg/mL) and 5 mM sodium L-  
50 ascorbate was mixed with an equal volume of a precipitant solution containing 0.2 M CaCl<sub>2</sub>, 0.1  
51 M sodium HEPES (pH 7.5), and 27%-33% polyethylene glycol (PEG) 4,000 in hanging drop  
52  
53  
54  
55  
56  
57



vapor diffusion trials. (*R*)-OH-TMAEP was incorporated via 1:1 (v:v) mixing of crystal drops with 20 mM (*R*)-OH-TMAEP prepared in the crystallization solution followed by a 24-h incubation at 25 °C. Crystals were prepared for data collection by cryoprotection in the well solution supplemented with 21% (v/v) glycerol, mounting on rayon loops, and flash freezing in liquid nitrogen.

The structure of the TmpB•Fe<sub>2</sub>•(*R*)-OH-TMAEP complex was solved by molecular replacement using the software package MOLREP<sup>54</sup> with the structure of PhnZ (PDB accession code 4MLM) as the search model. The final model contains four molecules of the protein in the asymmetric unit (ASU), with residues 8-195 in chain A, residues 8-194 in chain B, residues 7-76 and 85-195 in chains C and D, 6 Fe(II) ions (see explanation below), 4 Fe(III) ions, 2 (*R*)-OH-TMAEP (ligand TMO) molecules, and 261 water molecules. The diiron sites in chains A-D were modeled with one Fe(II) ion and one Fe(III) ion, because the mixed-valent cofactor accumulates to > 60% in solution when the diferric state is incubated with L-ascorbate, which was present during crystallization. However, the final oxidation state is not known and could be either Fe<sub>2</sub>(III/III) due to adventitious oxygen exposure during crystallization or Fe<sub>2</sub>(II/II) due to photoreduction during data collection. The (*R*)-OH-TMAEP is observed only in two of the four TmpB molecules in the ASU (chains C and D). The chains with substrate exhibit a disordered loop region, residues 77-84, near the active site. Conversely, this loop can be fully modeled in the chains that lack substrate; however, the electron density is weak and the temperature factors for this part of the model are high. The loop is found near a pair of adventitiously-bound iron ions that may be partially responsible for the ordering in the chains without substrate. This additional metal binding site, verified by an iron anomalous diffraction dataset but modeled at

1  
2  
3 50% occupancy for each site, is located between chains C and D (Figure S19).<sup>55</sup> Anomalous  
4  
5 diffraction Fourier maps were generated with CAD and FFT<sup>56-58</sup> of the CCP4 software suite.<sup>59</sup>  
6

7  
8 **<sup>57</sup>Fe Mössbauer spectroscopy.** Mössbauer spectra were recorded on SEECO (Edina, MN)  
9  
10 instruments that have been described previously.<sup>14</sup> The spectrometer used to acquire the weak-  
11  
12 field spectra is equipped with a Janis SVT-400 variable-temperature cryostat. The external  
13  
14 magnetic field was applied parallel to the  $\gamma$  beam. All isomer shifts are quoted relative to the  
15  
16 centroid of the spectrum of  $\alpha$ -iron foil at room temperature. Mössbauer spectra were simulated  
17  
18 using the WMOSS spectral analysis software (www.wmoss.org, WEB Research, Edina, MN).  
19  
20

21  
22 **Continuous-Wave (CW) EPR spectroscopy.** EPR spectra at X-Band (~9.5 GHz) were acquired  
23  
24 on a Bruker ESP-300 spectrometer equipped with an ER/4102 ST resonator (Bruker), an Oxford  
25  
26 Instruments continuous-helium-flow cryostat, and an Oxford Instruments temperature controller  
27  
28 (ITC 502). For all experiments, quartz tubes with 3 mm inner and 4 mm outer diameters were  
29  
30 used (QSI).  
31  
32

## 33 34 35 **RESULTS**

### 36 37 **The Fe/2OG oxygenase TmpA is a TMAEP hydroxylase**

38  
39 *Discovery of the TMAEP hydroxylation activity of TmpA.* The *Lc* TmpA protein shares 26%  
40  
41 sequence identity with *Homo sapiens* (*Hs*) BBOX and 33% identity with *Pseudomonas sp. AK-1*  
42  
43 (*Ps*) BBOX. The latter enzyme is, to the best of our knowledge, the only characterized bacterial  
44  
45 BBOX orthologue.<sup>39,60-62</sup> To evaluate the annotation of TmpA as a BBOX, the enzyme was  
46  
47 tested in a multiple-turnover reaction for the ability to hydroxylate  $\gamma$ bb. TmpA was found neither  
48  
49 to consume  $\gamma$ bb nor to produce the hydroxylated product, L-carnitine (Figure 1). By contrast, the  
50  
51  
52  
53  
54  
55  
56  
57  
58  
59  
60

positive-control enzyme, *Ps* BBOX, completely converted  $\gamma$ bb to L-carnitine under the same reaction conditions (Figure 1).

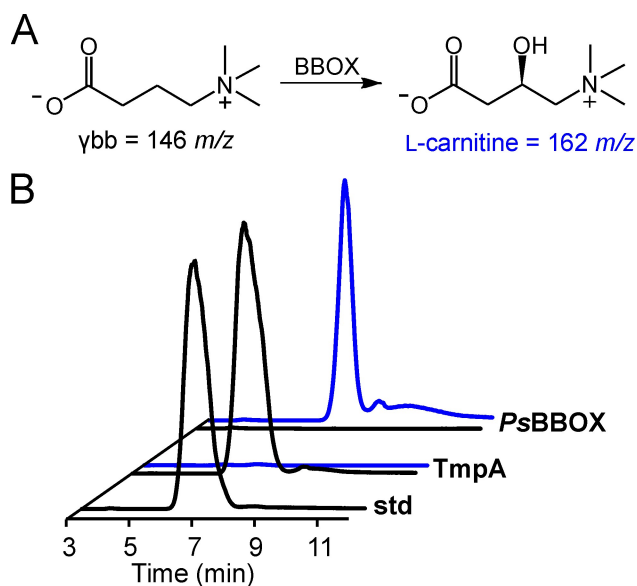


**Figure 1.** Assessment of the  $\gamma$ bb hydroxylase activities of TmpA and *Ps* BBOX. (A) The reaction catalyzed by BBOX. (B) LC-MS chromatograms monitoring  $\gamma$ bb (146  $m/z$ , black) and L-carnitine (162  $m/z$ , blue) after a 4-h incubation of 0.01 mM TmpA or *Ps* BBOX, 0.02 mM  $(\text{NH}_4)_2\text{Fe}(\text{SO}_4)_2$ , 0.2 mM sodium L-ascorbate, 1 mM 2OG and 1 mM  $\gamma$ bb.

The verified  $\gamma$ bb hydroxylation activity of *Ps* BBOX and complete absence of any such activity for TmpA prompted further scrutiny and comparison of their primary structures. A sequence similarity network (SSN)<sup>43,63</sup> was constructed for a Fe/2OG superfamily subset that included BBOX sequences and TmpA-like sequences (Figure S1). This subset also included the biochemically characterized enzyme,  $\epsilon$ -trimethyllysine hydroxylase (TMLH), which catalyzes the first step in eukaryotic L-carnitine biosynthesis.<sup>38,64</sup> TMLH, a close homologue of BBOX, was used as a rational benchmark for selection of a minimum pairwise alignment score that

1  
2  
3 generates isofunctional clusters (acting on the same substrate). Separation of the isofunctional  
4  
5 TMLH cluster from the BBOX cluster was achieved at a pairwise alignment score of  $10^{-65}$   
6  
7 (Figure S2). At this threshold, the BBOX and TmpA-like sequences also segregate into distinct  
8  
9 sub-clusters, with the nodes corresponding to the *Ps* BBOX and *Lc* TmpA proteins no longer  
10  
11 connected via an edge vector because their pairwise alignment score exceeds  $10^{-65}$ . The  
12  
13 separation of *Ps* BBOX and *Lc* TmpA into presumptively isofunctional clusters is consistent  
14  
15 with the experimental observation that they do not act on the same substrate. In a network  
16  
17 constructed from only bacterial sequences and with a slightly higher stringency for edges (Figure  
18  
19 S3), the clusters containing nodes for *Ps* BBOX and *Lc* TmpA become more isolated and adopt a  
20  
21 clustering pattern that reflects genomic context (Figure 2). Yellow nodes, which generally cluster  
22  
23 with *Lc* TmpA, represent proteins that are encoded adjacent to a gene encoding a TmpB-like  
24  
25 HD-domain protein and often downstream of a gene encoding a LysR-type transcription  
26  
27 regulator (Figure 2, yellow box). Within this cluster, a number of sequences are apparent protein  
28  
29 fusions of TmpA- and TmpB-like domains (orange nodes). Conversely, genes encoding proteins  
30  
31 represented by gray and green nodes lack the neighboring gene encoding an HD-domain protein.  
32  
33 Proteins represented by the green nodes are encoded in gene neighborhoods similar to the  $\gamma$ bb-  
34  
35 degradation operon previously characterized in *Ps*.<sup>39</sup> This operon encodes the *Ps* BBOX enzyme,  
36  
37 as well as proteins involved in betaine uptake and further degradation of L-carnitine to glycine  
38  
39 betaine (Figure 2, green box).<sup>39</sup> Thus, the proteins represented by green nodes are likely to be  
40  
41 authentic BBOX enzymes that enable bacterial  $\gamma$ bb assimilation. The clear dichotomy between  
42  
43 the genomic contexts of TmpA-clustered proteins and those clustered with *Ps* BBOX is  
44  
45 consistent with their use of different substrates, as shown experimentally for *Lc* TmpA.  
46  
47  
48  
49  
50  
51  
52  
53  
54  
55  
56  
57  
58  
59  
60

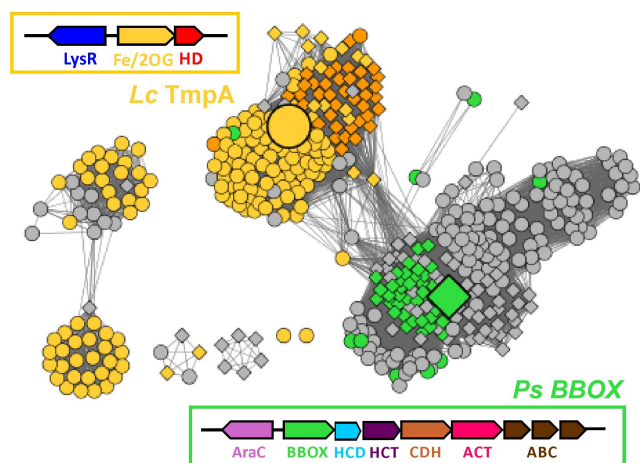


**Figure 2.** Sequence similarity network (SSN) illustrating divergence of BBOX-like and TmpA-like proteins. The clusters of bacterial protein sequences shown here are derived from the IPR003819 SSN (Figures S1-3). The nodes represent protein sequences with > 90% identity. Edges between the nodes represent pairwise alignment scores of  $< 10^{-71}$  (corresponding to ~ 33% sequence identity). The large yellow circle and green diamond represent *Lc* TmpA and *Ps* BBOX, respectively. Orange nodes represent predicted fusion proteins with both TmpA- and TmpB-like domains. Diamond shaped nodes represent sequences with an N-terminal Zn(II)-binding motif (see discussion). The yellow and green boxes summarize the genomic context of proteins represented by the yellow and green nodes, respectively. Other designations: LysR, LysR-type transcription regulator; AraC, AraC-type transcription regulator; CDH, carnitine dehydrogenase; HCT, 4-hydroxybenzoyl-CoA thioesterase; HCD, 3-hydroxybutyryl-CoA dehydrogenase; ACT, Acetyl-CoA acetyltransferase/thiolase; ABC, ABC-type glycine/betaine transporter.

We initially predicted that the substrate for TmpA might be structurally similar to the  $\gamma$ bb substrate of BBOX and therefore tested various analogues of that compound. None of the analogues most similar in structure to  $\gamma$ bb, possessing both the trimethylammonium and

1  
2  
3 carboxylate groups, were consumed by TmpA (Figure S5). We noted that the BBOX active site  
4 residues that interact with the quaternary amine of  $\gamma$ bb (*vide infra*) are, in fact, conserved (or  
5 conservatively substituted) in TmpA sequences. We therefore considered that the TmpA  
6 substrate would retain this structural element but have a different substituent replacing the  
7 carboxylate group. TmpA was found to act, in the presence of its presumptive co-substrates,  
8 2OG and O<sub>2</sub>, on the quaternary ammonium-containing compound phosphocholine (Figure S6).  
9 The analogy of the genomic synteny of the TmpA/B pair to that of the phosphonate-degrading  
10 PhnY/Z pair suggested the possibility that the former pair might also degrade a phosphonate  
11 compound. Thus, we tested the naturally occurring phosphonate analogue of phosphocholine, 2-  
12 (trimethylammonio)ethylphosphonate (TMAEP) and observed efficient consumption (200  
13 turnovers) under the same assay conditions (Figure 3). TMAEP was completely converted to a  
14 product with a distinct <sup>31</sup>P-NMR chemical shift and an *m/z* of +16 relative to that of the  
15 substrate, suggestive of substrate hydroxylation (Figure 3). By NMR analysis (Figure S4), we  
16 determined the purified product to be 1-hydroxy-2-(trimethylammonio)ethylphosphonate (OH-  
17 TMAEP). The configuration of C1 (*R*) was evident from the X-ray crystal structures of the  
18 TmpA•product and TmpB•substrate complexes (described below). The C1 configuration  
19 matches that generated by PhnY in the cognate intermediate of the previously identified pathway  
20 for degradation of the unmethylated analog, 2-AEP.<sup>22</sup> Hydroxylation of TMAEP was dependent  
21 on the presence of TmpA, 2OG, and O<sub>2</sub> (Figure S7), and tight coupling between succinate  
22 production and TMAEP consumption was observed, with a stoichiometry close to the theoretical  
23 value of unity (Figure S7). By contrast, no conversion of TMAEP under analogous conditions  
24 was observed upon incubation with PhnY (Figure 3), which natively hydroxylates the  
25  
26  
27  
28  
29  
30  
31  
32  
33  
34  
35  
36  
37  
38  
39  
40  
41  
42  
43  
44  
45  
46  
47  
48  
49  
50  
51  
52  
53  
54  
55  
56  
57  
58  
59  
60

corresponding primary amine analogue (2-AEP). *Ps* BBOX converted only a small fraction (< 10%) of the TMAEP in a 4-h incubation (Figure 3).

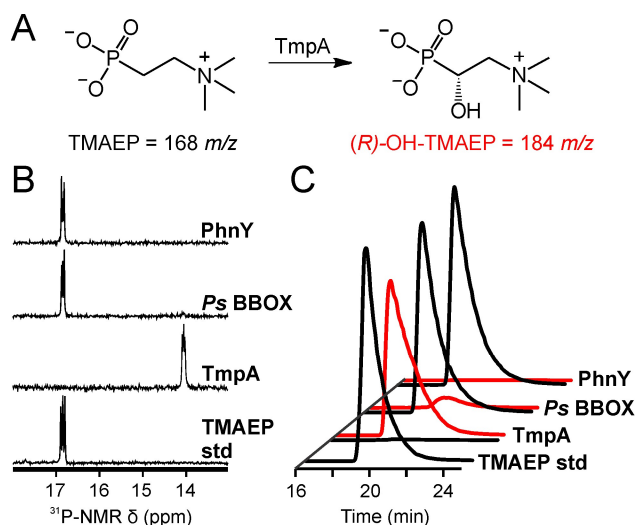


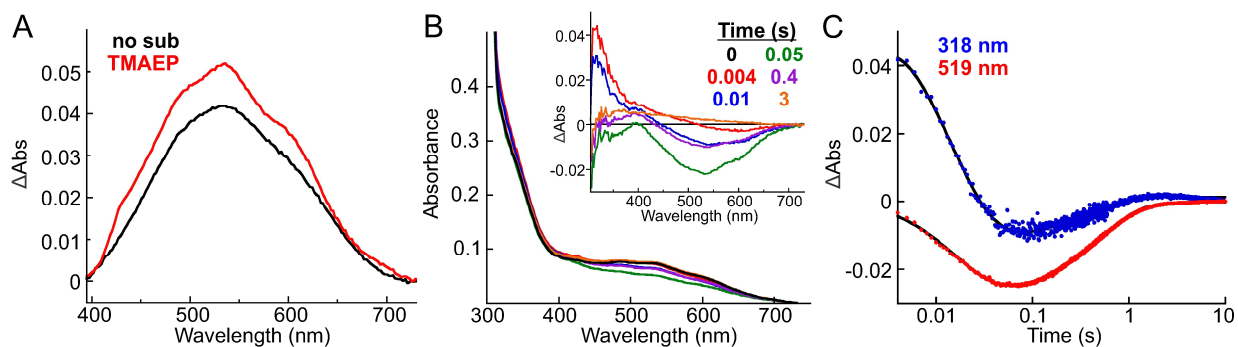
**Figure 3.** Activities of selected Fe/2OG oxygenases toward TMAEP. (A) The chemical transformation catalyzed by TmpA. (B) <sup>31</sup>P-NMR spectra and (C) LC-MS chromatograms after a 4-h incubation of a solution containing 0.01 mM TmpA, PhnY or *Ps* BBOX with 0.02 mM (NH<sub>4</sub>)<sub>2</sub>Fe(SO<sub>4</sub>)<sub>2</sub>, 0.2 mM L-ascorbate, 3 mM 2OG and 2 mM TMAEP. The triplet splitting in the <sup>1</sup>H-decoupled <sup>31</sup>P-NMR spectra of the TMAEP substrate and (R)-OH-TMAEP product in panel B is presumed to result from the <sup>14</sup>N nucleus on C1. The reason it is present in the spectrum of the *N*-trimethylated compound, but not those of the di- and unmethylated analogs, is not clear and is discussed more in the *Supporting Information*.

As a foundation for assessing the enzyme's specificity for this substrate, the capacity of TMAEP to bind to TmpA and trigger its reaction with O<sub>2</sub> were probed by UV-visible absorption spectroscopy. In the absence of substrate, the ternary TmpA•Fe(II)•2OG complex exhibited the usual visible absorption feature at 530 nm (Figure 4A), attributed in previous studies on other

1  
2  
3 Fe/2OG oxygenases to a metal-to-2OG charge-transfer transition.<sup>65</sup> Mixing of this complex with  
4  
5 limiting O<sub>2</sub> resulted in only a very sluggish reaction, marked by slow development of an  
6  
7 absorption feature centered at ~ 350 nm (Figure S8). These spectral changes likely reflect  
8  
9 unproductive oxidation of the Fe(II) cofactor to Fe(III), as observed for other Fe/2OG  
10  
11 enzymes.<sup>14,66</sup> Addition of TMAEP to an anoxic solution of the ternary TmpA•Fe(II)•2OG  
12  
13 complex elicited additional structure in the MLCT band, as well as small but reproducible hyper-  
14  
15 and hypsochromic shifts (Figure 4A), reflecting the effect of TMAEP binding on the geometry  
16  
17 and electronic structure of the cofactor.<sup>67-69</sup> Mixing of the resultant quaternary  
18  
19 TmpA•Fe(II)•2OG•TMAEP complex with limiting O<sub>2</sub> led to rapid, transient changes reflective  
20  
21 of a single enzyme turnover (Figure 4B). The 520-nm feature of the reactant complex decayed  
22  
23 and re-developed (Figure 4B, C), signifying conversion of the reactant complex to a transparent  
24  
25 state – most likely the TmpA•Fe(II)•succinate•(*R*)-OH-TMAEP product complex<sup>70</sup> – followed by  
26  
27 re-formation of the reactant complex. Non-linear regression analysis of the kinetic traces  
28  
29 (described in the Experimental Section) yielded apparent first-order rate constants of 59 s<sup>-1</sup> for  
30  
31 the decay phase and 2.0 s<sup>-1</sup> for the re-development phase. Additionally, a feature with an  
32  
33 apparent maximum of 318 nm developed by the time of the first reliable spectrum (4 ms; Figure  
34  
35 4B, red trace) and decayed with a rate constant (67 s<sup>-1</sup>) not significantly different from the larger  
36  
37 value extracted from analysis of the 520-nm traces (Figure 4C). A final re-development phase  
38  
39 had an observed rate constant equivalent to that for re-development of the visible feature of the  
40  
41 reactant complex. These transient UV absorption spectra and kinetic traces reflect the rapid  
42  
43 (nearly in the dead-time of the stopped-flow instrument) accumulation of the ferryl intermediate,  
44  
45 its slower decay to a product complex, and the overall rate-limiting re-formation of the reactant  
46  
47 complex upon dissociation of the products and re-binding of 2OG and TMAEP (Scheme 1). We  
48  
49  
50  
51  
52  
53  
54  
55  
56  
57  
58  
59  
60



1  
2  
3 have previously documented similar kinetic schemes for multiple other Fe/2OG  
4 oxygenases.<sup>14,66,71-74</sup>  
5  
6  
7  
8  
9



10  
11  
12  
13  
14  
15  
16  
17  
18  
19  
20  
21  
22 **Figure 4.** Ultraviolet-visible absorption data showing binding of TMAEP to TmpA•Fe(II)•2OG  
23 and triggering of O<sub>2</sub> addition. (A) Difference absorption spectra associated with binding of 2OG  
24 (5 mM) to the TmpA•Fe(II) complex [0.6 mM TmpA, 0.5 mM (NH<sub>4</sub>)<sub>2</sub>Fe(SO<sub>4</sub>)<sub>2</sub>] in the absence  
25 of substrate (black) and presence of 5 mM TMAEP (red). (B) Stopped-flow absorption spectra  
26 acquired after mixing at 5 °C of a solution of 1.2 mM TmpA, 1 mM (NH<sub>4</sub>)<sub>2</sub>Fe(SO<sub>4</sub>)<sub>2</sub>, 10 mM  
27 2OG and 10 mM TMAEP with an equal volume of air-saturated 50 mM sodium HEPES buffer,  
28 pH 7.5 (~ 0.4 mM O<sub>2</sub> at 5 °C). The inset shows the absorption spectra at indicated time points  
29 after subtraction of the spectrum of the TmpA•Fe(II)•2OG•TMAEP complex. (C) Kinetic traces  
30 at 318 nm (blue dots) and 519 nm (red dots) extracted from the time-dependent spectra in panel  
31 B. The solid black lines are regression fits to the data, as described in the Experimental Section.  
32  
33  
34  
35  
36  
37  
38  
39  
40  
41  
42  
43  
44  
45  
46  
47  
48  
49  
50  
51  
52  
53  
54  
55  
56  
57  
58  
59  
60

*Examining the substrate specificity of TmpA.* Structural analogues of TMAEP were tested for their ability to bind to TmpA, trigger O<sub>2</sub> activation, and serve as substrates in multiple-turnover activity assays. A panel of natural and synthetic organophosphonate compounds was screened to examine whether the phosphonate alone was sufficient for substrate processing. TmpA was

1  
2  
3 unable to consume the vast majority of these compounds, with the exceptions of 2-AEP and 3-  
4 aminopropylphosphonate (the latter not known to occur in nature), which were processed only  
5 very inefficiently (Figures S9, S10). Compounds with a hydroxyl, carboxylate, or sulfonate  
6 group in place of the phosphonate (e.g., choline,  $\gamma$ bb,  $\gamma$ bb-3, taurine,  $\gamma$ -aminobutyric acid, and  $\beta$ -  
7 alanine) were also not detectably consumed after a 4-h incubation with TmpA, Fe(II), and co-  
8 substrates (Figure S10). Addition of any one of the latter set of analogues to the  
9 TmpA•Fe(II)•2OG ternary complex did not perturb the absorption spectrum (Figure S11),  
10 suggesting that none binds with affinity comparable to that of TMAEP. Furthermore, none of  
11 these analogues triggered the reaction with O<sub>2</sub>, demonstrated by their failure to promote either  
12 the rapid loss of the 520-nm feature of the reactant complex or the development of the transient  
13 318-nm absorption feature of the ferryl intermediate (Figure S11).  
14  
15  
16  
17  
18  
19  
20  
21  
22  
23  
24  
25  
26  
27

28 Analogues retaining the phosphonate moiety but having reduced degrees of amine  
29 methylation were also examined as substrates for TmpA and were found to be poorer than  
30 TMAEP. Addition of 2-(dimethylamino)ethylphosphonate (DMAEP) to the TmpA•Fe(II)•2OG  
31 ternary complex induced a shift in the absorption spectrum similar to that caused by TMAEP  
32 (Figure 5A, blue). Subsequent mixing of the TmpA•Fe(II)•2OG•DMAEP complex with limiting  
33 O<sub>2</sub> resulted in the spectral changes characteristic of a single turnover, as observed for TMAEP  
34 (Figure 5B, blue). However, the observed rate constant for the decay phase at 520 nm was  
35 approximately four times less ( $k_{obs} = 13 \text{ s}^{-1}$ ) than that observed with TMAEP. A new species with  
36 an increased  $m/z$  of +16 relative to that of the substrate was detected by LC-MS (Figure S10),  
37 and the presence of a new peak with a distinct <sup>31</sup>P-NMR chemical shift (Figure 5C) suggested  
38 hydroxylation of the dimethyl analogue. In multiple-turnover reactions with low concentrations  
39 of TmpA, the turnover frequency with DMAEP ( $\nu_0/[E] = 0.43 \text{ s}^{-1}$ ) was 1.6-fold less than with  
40  
41  
42  
43  
44  
45  
46  
47  
48  
49  
50  
51  
52  
53  
54  
55  
56  
57  
58  
59  
60

1  
2  
3 TMAEP ( $v_0 = 0.67 \text{ s}^{-1}$ ). Such a modest difference in rate compelled us to assess more directly the  
4 enzyme's preference for the *N*-trimethyl versus the *N*-dimethyl substrate in a competition assay  
5  
6 with the two compounds present in equal concentration. TmpA consumed exclusively TMAEP at  
7  
8 early incubation times and began to process DMAEP only after TMAEP was almost entirely  
9  
10 depleted (Figure 6B), consistent with a preference for the *N*-trimethyl substrate. With the  
11  
12 corresponding unmethylated compound, 2-AEP, TmpA was found to carry out fewer than 10  
13  
14 turnovers after a 4-h incubation with excess 2OG and  $\text{O}_2$  (Figure 5C and S11). Accordingly,  
15  
16  
17  
18  
19  
20  
21  
22  
23  
24  
25  
26  
27  
28  
29  
30  
31  
32  
33  
34  
35  
36  
37  
38  
39  
40  
41  
42  
43  
44  
45  
46  
47  
48  
49  
50  
51  
52  
53  
54  
55  
56  
57  
58  
59  
60

addition of 2-AEP to the TmpA•Fe(II)•2OG complex elicited a less pronounced shift in its absorption spectrum than for TMAEP or DMAEP (Figure 5A, green), and no detectable triggering of the  $\text{O}_2$  reaction was observed (Figure 5B, green). These comparisons show that the presence of three *N*-methyl groups is important for high-affinity, functional binding in the active site.

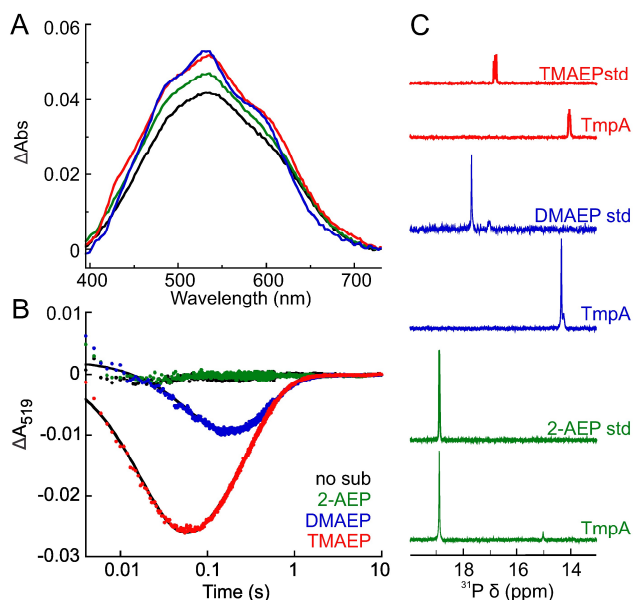


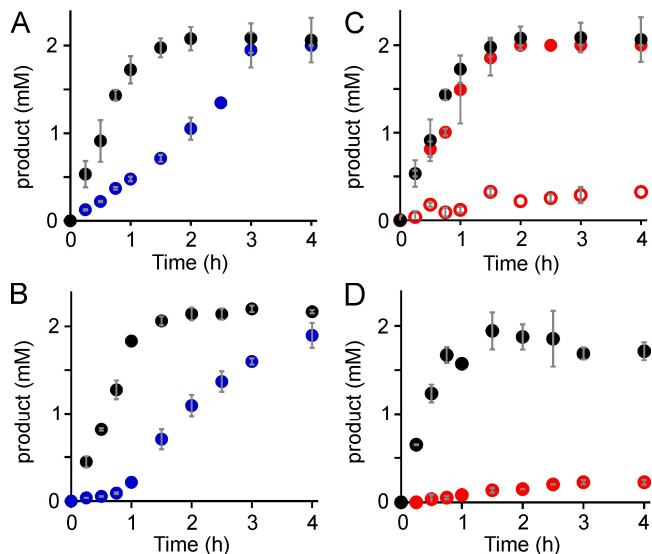
**Figure 5.** Activity of TmpA toward TMAEP analogues with varying degrees of *N*-methylation.

(A) Absorption difference spectra caused by binding of 2OG (5 mM) to the TmpA•Fe(II)

1  
2  
3 complex [0.6 mM TmpA, 0.5 mM (NH<sub>4</sub>)<sub>2</sub>Fe(SO<sub>4</sub>)<sub>2</sub>] in the absence of a substrate (black) and in  
4  
5 the presence of 5 mM TMAEP (red), DMAEP (blue) or 2-AEP (green). (B) Kinetic traces at 519  
6  
7 nm after mixing of the solutions described in panel A with air-saturated 50 mM sodium HEPES  
8  
9 buffer, pH 7.5 (~ 0.2 mM O<sub>2</sub> final at 5 °C). The solid black lines are non-linear regression fits to  
10  
11 the data, as described in the Experimental Section. (C) <sup>31</sup>P-NMR spectra of reaction samples  
12  
13 after a 4 h incubation of a solution of 0.01 mM TmpA, 0.02 mM (NH<sub>4</sub>)<sub>2</sub>Fe(SO<sub>4</sub>)<sub>2</sub>, 0.2 mM  
14  
15 sodium ascorbate, 3 mM 2OG and 2 mM of either TMAEP (red), DMAEP (blue), or 2-AEP  
16  
17 (green).  
18  
19  
20  
21  
22  
23

24 As noted previously, TmpA degrades the phosphoester analogue of TMAEP,  
25  
26 phosphocholine (PC). The reaction produces phosphate and glycine betaine aldehyde, the former  
27  
28 determined by its <sup>31</sup>P-NMR chemical shift and the latter by its *m/z* in LC-MS analysis (Figure  
29  
30 S6). The observed products presumably result from hydroxylation at C1 of PC followed by  
31  
32 elimination of phosphate. This reaction is robustly catalytic, such that a 1-h incubation of PC  
33  
34 with TmpA in the presence of excess 2OG and O<sub>2</sub> resulted in its complete consumption (100  
35  
36 turnovers), as observed with TMAEP under identical conditions (Figure 6C). However, the  
37  
38 turnover frequency was found to be less with PC ( $v_0/[E] = 0.074 \text{ s}^{-1}$  at 3 °C) than with TMAEP  
39  
40 by a factor of ~ 9. Additionally, no changes to the optical spectrum were seen upon reaction of  
41  
42 the presumptive TmpA•Fe(II)•2OG•PC quaternary complex with O<sub>2</sub> (Figure S11), suggesting  
43  
44 that the initial O<sub>2</sub>-addition step is slow compared to subsequent events leading to re-formation of  
45  
46 the reactant complex. In a competition experiment, TMAEP was first consumed to completion, at  
47  
48 which point PC was then slowly consumed (Figure 6D), clearly demonstrating a preference for  
49  
50 the phosphonate compound. Furthermore, the TmpA reaction with PC was inhibited in this  
51  
52  
53  
54  
55  
56  
57  
58  
59  
60

1  
2  
3 competition assay compared with a reaction containing only PC (i.e., in the absence of TMAEP;  
4 compare Figure 6C, D). The inhibition was presumed to be caused by the TMAEP product, (*R*-  
5 OH-TMAEP, which was confirmed by including it at a high concentration in a reaction with PC  
6 as the sole substrate (Figure 6C).  
7  
8  
9  
10  
11  
12  
13  
14



33 **Figure 6.** Evaluation of relative specificity of TmpA for TMAEP and either DMAEP or PC by  
34 direct competition. All reactions were performed at 3 °C and contained 0.02 mM TmpA, 0.03  
35 mM (NH<sub>4</sub>)<sub>2</sub>Fe(SO<sub>4</sub>)<sub>2</sub>, 0.4 mM sodium ascorbate, 6 mM 2OG and 2 mM of each substrate. (A)  
36 mM (NH<sub>4</sub>)<sub>2</sub>Fe(SO<sub>4</sub>)<sub>2</sub>, 0.4 mM sodium ascorbate, 6 mM 2OG and 2 mM of each substrate. (A)  
37 Control reactions containing either TMAEP (black) or DMAEP (blue) in the absence of the other  
38 compound, monitoring corresponding hydroxylated products by LC-MS. (B) Competition  
39 reactions containing both TMAEP and DMAEP, monitoring corresponding hydroxylated  
40 products by LC-MS. (C) Control reactions containing either TMAEP (black) or PC (filled red),  
41 monitoring (*R*)-OH-TMAEP production and PC consumption, respectively, by LC-MS. The open  
42 red circles are the concentration of PC consumed, detected by LC-MS, from a reaction  
43 containing PC and 2 mM (*R*)-OH-TMAEP. (D) Competition reactions containing both TMAEP  
44  
45  
46  
47  
48  
49  
50  
51  
52  
53  
54  
55  
56  
57  
58  
59  
60

1  
2  
3 and PC, monitoring (*R*)-OH-TMAEP and phosphate products by <sup>31</sup>P-NMR because PC and (*R*)-  
4  
5 OH-TMAEP have the same *m/z* and similar retention times.  
6  
7  
8  
9

10 *Structural basis for TmpA substrate specificity.* The x-ray crystal structure of the  
11  
12 TmpA•Fe(II)•2OG complex was solved to a resolution of 1.73 Å by molecular replacement  
13  
14 using the C-terminal catalytic domain of the *Hs* BBOX structure (PDB accession code 3O2G<sup>75</sup>)  
15  
16 as the search model. As forecast by the sequence similarity that led to the misannotation of  
17  
18 TmpA as a BBOX, the two proteins have a number of structural features in common. The overall  
19  
20 topologies are remarkably similar (Figures 7, S12), with a root-mean-squared standard deviation  
21  
22 (rmsd) of 2.5 Å for 355 C $\alpha$ -atoms.<sup>76</sup> The tertiary structure of the TmpA monomer consists of an  
23  
24 N-terminal dimerization domain (residues 1-96), a short linker (97-100), and a C-terminal  
25  
26 catalytic domain containing the eight-stranded  $\beta$ -sandwich (cupin) fold characteristic of Fe/2OG  
27  
28 oxygenases (Figure S12).<sup>2,11,77</sup> In both TmpA and *Hs* BBOX, the N-terminal domain facilitates  
29  
30 assembly of a symmetric head-to-tail dimer via its interface with the C-terminal domain of the  
31  
32 other monomer (Figure 7). Analysis by size exclusion chromatography confirmed that this  
33  
34 quaternary structure of TmpA is also present in solution (Figure S13). The N-terminal domains  
35  
36 of TmpA and *Hs* BBOX are structurally homologous, despite sharing < 20% sequence identity,  
37  
38 and are composed of two three-strand antiparallel  $\beta$ -sheets with an intervening  $\alpha/\beta$  insertion  
39  
40 (Figures S12, S14). However, whereas *Hs* BBOX harbors an essential Zn(II) ion in the  $\alpha/\beta$   
41  
42 insertion,<sup>75</sup> TmpA lacks the CxCxxC...H sequence motif required for metal binding, and a  
43  
44 divalent cation is not observed in its N-terminal domain (Figure S14).  
45  
46  
47  
48  
49  
50

51 Structures of TmpA were also solved with the TMAEP substrate (1.70 Å resolution) and  
52  
53 (*R*)-OH-TMAEP product (1.78 Å resolution) bound. In all three of the resulting models, the  
54  
55  
56  
57  
58  
59  
60

1  
2  
3 active site is located in the C-terminal domain of TmpA and contains an Fe(II) center  
4 coordinated by residues His198, Asp200, and His344 in the expected facial triad geometry  
5  
6 (Figures 7, S15).<sup>12,13</sup> The dimer quaternary structure of TmpA affords two independent views of  
7  
8 the active site in the asymmetric unit. However, in one of the two monomers (chain B), the  
9  
10 catalytic center is occluded by crystal packing interactions (Figure S16). The lattice artifact locks  
11  
12 an active-site lid loop into an open/disordered conformation in chain B, preventing 2OG and the  
13  
14 primary substrate/product from binding (Figure S15). In chain A of both the TMAEP-bound and  
15  
16 TMAEP-free structures, 2OG coordinates in bidentate mode to the iron center (Figures 7, S15)  
17  
18 and is stabilized by a salt-bridge interaction with the side chain of conserved residue Arg352. In  
19  
20 the absence of the primary substrate, an octahedral Fe(II) coordination geometry is completed by  
21  
22 a water ligand axial to His344, and a sulfate ion from the crystallization solution occupies the  
23  
24 phosphonate binding site described below (Figure S15). In the TMAEP-bound structure, the  
25  
26 Fe(II) ion has lost the axial water ligand, presumably opening the position for dioxygen addition  
27  
28 to initiate the reaction (Figures 7, S15). Structural comparisons show that binding of TMAEP is  
29  
30 accompanied by inward collapse of two core beta strands ( $\beta 2$  and  $\beta 3$ ) that immediately precede  
31  
32 the HxD metal-binding sequence motif (Figure S16). In addition, the loop connecting these beta  
33  
34 strands (residues 179-196) becomes ordered and closes over the active site (described below) to  
35  
36 shield it from solvent (Figure S16). Interestingly, this structure differs from the corresponding  
37  
38 dynamic lid regions of many other Fe/2OG enzymes (Figure S17). This distinction is likely  
39  
40 mandated by the location of the N-terminal domain of the other TmpA protomer, which overlaps  
41  
42 with the typical lid-loop binding site. Closure of the unorthodox TmpA lid-loop around the  
43  
44 TMAEP substrate results in formation of an extended water-mediated H-bonding network  
45  
46 involving the substrate phosphonate group, the lid-loop backbone, and residues in the  $\alpha/\beta$   
47  
48  
49  
50  
51  
52  
53  
54  
55  
56  
57  
58  
59  
60

1  
2  
3 insertion of the N-terminal domain (Figure S16). This analysis suggests that the TmpA N-  
4 terminal domain functions in substrate binding by stabilizing the closed conformation.  
5  
6

7  
8 The active site residues that interact with TMAEP form a pocket similar to that observed  
9  
10 in *Hs* BBOX for  $\gamma$ bb, particularly in the vicinity of the quaternary ammonium group (Figure 7).  
11 An aromatic cage is formed by the side chains of Tyr173, Phe177, and Tyr190 around the -  
12  $N^+(CH_3)_3$  moiety (Figure 7). Tyr190 is located in the dynamic lid loop (Figure S16), consistent  
13 with a role for this structural motif in substrate binding/specificity. The faces of their aromatic  
14 rings engage in cation- $\pi$  interactions, which are commonly involved in binding of substrates with  
15 quaternary ammonium groups.<sup>78</sup> The phosphonate dianion forms hydrogen-bonding interactions  
16 with a water molecule and the side chains of Asn187, Asn201, Tyr203, and Asn286 (Figure  
17 S16). The phosphonate group also interacts electrostatically with Arg288 (Figure 7), which is a  
18 key player in the extended H-bonding network involving the N-terminal domain of the opposite  
19 monomer (Figure S16). The fact that Arg288 is one of the few residues in the substrate-binding  
20 pocket that is not conserved in actual BBOX sequences (e.g., *Hs* Ala294) suggests that it is  
21 important in conferring specificity for the phosphonate moiety. These substrate interactions poise  
22 the C1 *pro-S* hydrogen of TMAEP above the open axial coordination site of the iron center  
23 (Figure 7), with the carbon at a distance of 4.2 Å. The product-bound structure (Figure S15)  
24 reveals clear electron density for a hydroxyl group appended to TMAEP at the C1 position with  
25 *R* stereochemistry [(*R*)-OH-TMAEP], consistent with the expected retention of configuration in  
26 the C–O-coupling step following transfer of the *pro-S* hydrogen to the ferryl complex. We  
27 presume that hydroxylation resulted here from adventitious O<sub>2</sub> exposure leading to turnover,  
28 during crystallization. Consistent with this interpretation, the electron density in the equatorial  
29 plane cannot be modeled well by 2OG and most likely represents a mixture of succinate  
30  
31  
32  
33  
34  
35  
36  
37  
38  
39  
40  
41  
42  
43  
44  
45  
46  
47  
48  
49  
50  
51  
52  
53  
54  
55  
56  
57  
58  
59  
60



(produced by turnover) and acetate (present in the synthetic TMAEP) (Figure S15). Together, the structures of TmpA in the substrate-free, substrate-bound, and product-bound states reveal dynamic changes in the protein structure that create a substrate pocket that is subtly but functionally different from that in BBOX.

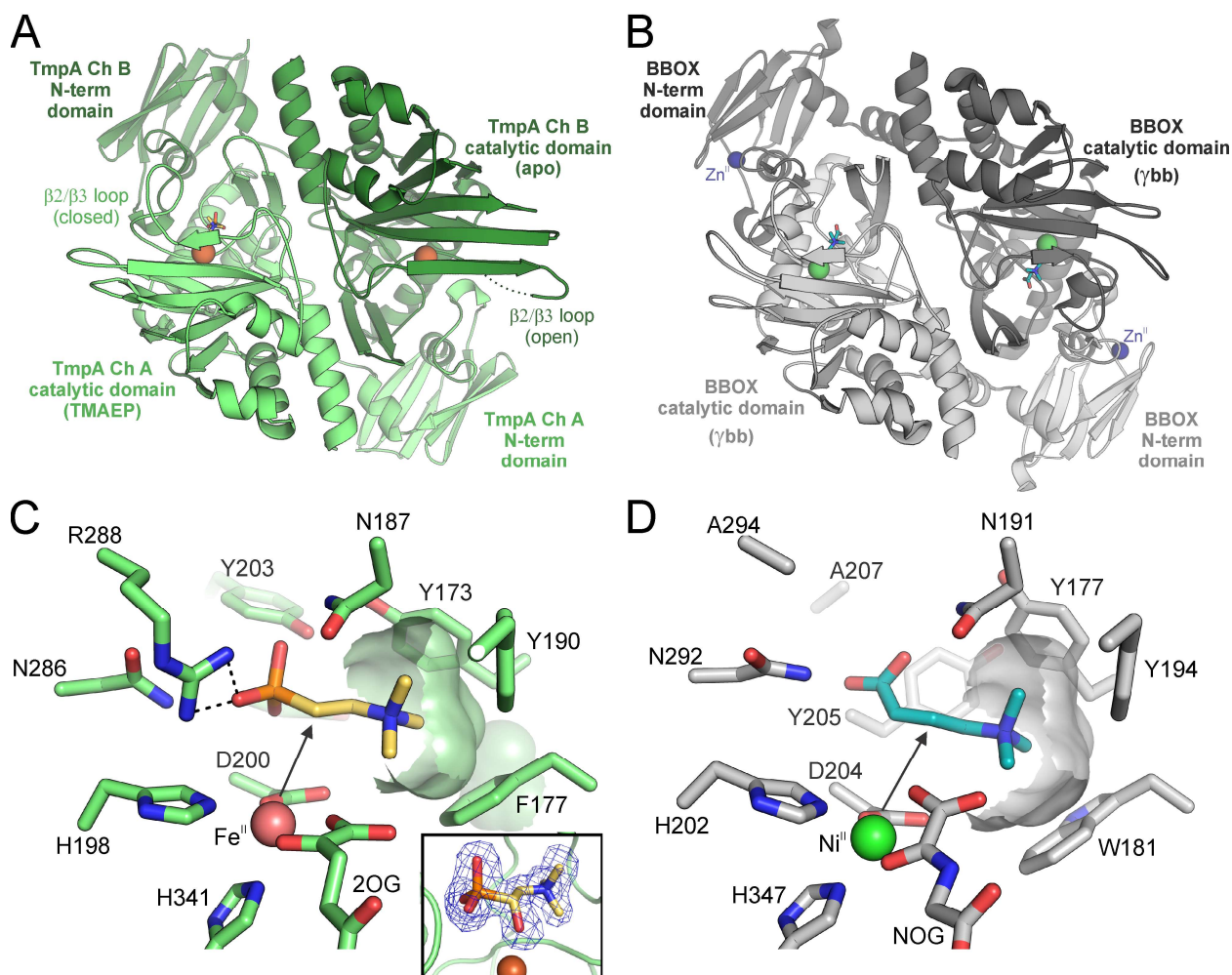


**Figure 7.** Structural comparison of *Lc* TmpA and *Hs* BBOX. (A) Homodimeric quaternary structure of TmpA with chain A in light green and chain B in dark green. Fe(II) ions are shown as brown spheres. (B) Homodimeric quaternary structure of *Hs* BBOX (PDB accession code 3MS5) with chain A in dark gray and chain B in light gray. The Zn(II) and Ni(II) ions are shown

1  
2  
3 as blue and green spheres, respectively. (C) Active site of chain A in the TmpA substrate-bound  
4 structure, showing the co-substrate (2OG), amino acid side chains, and TMAEP (yellow) in stick  
5 format. Electrostatic interactions are designated by black dashed lines and the black arrow  
6 identifies the position of hydroxylation. The inset shows the  $F_o-F_c$  omit map contoured at  $3.0\sigma$   
7 (blue mesh) and atomic model for (*R*)-OH-TMAEP (yellow sticks) in chain A of the TmpA  
8 product-bound structure. (D) Active site in the substrate-bound structure of *Hs* BBOX (PDB  
9 accession code 3MS5), showing the co-substrate analog, *N*-oxalylglycine (NOG), amino acids  
10 side chains, and  $\gamma$ bb (blue) in stick format.  
11  
12  
13  
14  
15  
16  
17  
18  
19  
20  
21  
22  
23

### 24 **TmpB is an HD-domain mixed-valent diiron oxygenase acting upon (*R*)-OH-TMAEP.**

25  
26 *Characterization of the TmpB mixed-valent diiron cofactor.* The genomic synteny of TmpA and  
27 TmpB and the precedent provided by the PhnY/PhnZ pathway led us to anticipate that TmpB  
28 might use the product of the TmpA reaction as its substrate. This product, (*R*)-OH-TMAEP, is  
29 the trimethylammonium analogue of the PhnZ substrate, (*R*)-OH-AEP. Moreover, *Lc* TmpB  
30 shares 32% sequence identity with PhnZ (from *uncultured bacterium HF130\_AEPn\_1*),  
31 including conservation of its extended metal-binding sequence motif (Figure S18), suggesting  
32 that it could be a related HD-domain mixed-valent diiron oxygenase (HD-MVDO),<sup>21,22</sup> despite  
33 having been annotated as a phosphodiesterase.  
34  
35  
36  
37  
38  
39  
40  
41  
42  
43

44 The two known HD-MVDOs, PhnZ and MIOX, both use mixed-valent [Fe<sub>2</sub>(II/III)] diiron  
45 cofactors to activate O<sub>2</sub> for four-electron oxidation reactions. We first used atomic emission  
46 spectroscopy (ICP-AES) and Mössbauer spectroscopy to determine both the nuclearity of the  
47 presumptive TmpB metallocofactor and its stable oxidation states. The His<sub>6</sub>-tagged protein  
48 emerged from over-expression in *E. coli* and purification by immobilized metal-ion affinity  
49  
50  
51  
52  
53  
54  
55  
56  
57  
58  
59  
60

1  
2  
3 chromatography with 1.0-1.3 molar equivalents of Fe and undetectable levels of other transition  
4 metals bound. TmpB enriched in  $^{57}\text{Fe}$  (> 95 %) was incubated with chemical oxidants and  
5 reductants to probe the accessible oxidation states of the cofactor. The 120-K/0-T spectrum of  
6 the sample treated with the oxidant potassium ferricyanide (Figure 8A) is a single quadrupole  
7 doublet with parameters (isomer shift,  $\delta$ , of 0.49 mm/s and quadrupole splitting parameter,  $\Delta E_Q$ ,  
8 of 0.84 mm/s) typical of high-spin Fe(III) ions with N/O coordination. The presence of a  
9 quadrupole doublet feature in the 4.2-K/53-mT spectrum of the same sample (Figure S19)  
10 indicates that the cofactor has an integer-spin electronic ground state, which can be rationalized  
11 by antiferromagnetic coupling of two high-spin ferric ions ( $S = 5/2$ ) in a dinuclear cluster to give  
12 a total electron spin ( $S_{\text{total}}$ ) of 0.<sup>55</sup> The 120-K/0-mT spectrum (Figure 8B) of the sample treated  
13 with sodium dithionite is slightly heterogenous and could be best fit as a superposition of two  
14 quadrupole doublets with parameters ( $\delta_1 = 1.24$  mm/s,  $\Delta E_{Q1} = 3.25$  mm/s, Area = 0.76;  $\delta_2 = 1.24$   
15 mm/s,  $\Delta E_{Q2} = 2.50$  mm/s, Area = 0.23) characteristic of high-spin ferrous ions with O/N ligands,  
16 suggesting conversion of the as-isolated sample to the fully reduced  $\text{Fe}_2(\text{II}/\text{II})$  state by the strong  
17 reductant. By contrast, treatment of the as-isolated TmpB with the milder reductant, L-ascorbate,  
18 gave a different cofactor form. Its 4.2-K/53-mT spectrum is dominated by a broad multi-line  
19 signal (Figure S20), similar to that observed for the  $\text{Fe}_2(\text{II}/\text{III})$  complex of MIOX, which has a  
20 ground state with  $S_{\text{total}} = 1/2$ .<sup>79</sup> At higher temperature (120 K) and in the absence of an externally  
21 applied magnetic field, the paramagnetic features collapsed into quadrupole doublets (Figure  
22 S20). In this 120-K/0-T spectrum, a minor contribution (22 %) of a diferrous form was evident  
23 from the presence of a partially resolved feature matching the position of the corresponding high-  
24 energy line in the reference spectrum of the pure  $\text{Fe}_2(\text{II}/\text{II})$  form; it was subtracted from the  
25 experimental spectrum to resolve the superimposed contributions of the other components  
26  
27  
28  
29  
30  
31  
32  
33  
34  
35  
36  
37  
38  
39  
40  
41  
42  
43  
44  
45  
46  
47  
48  
49  
50  
51  
52  
53  
54  
55  
56  
57  
58  
59  
60

(Figure S20). The resultant spectrum could then be accounted for as a superposition of three quadrupole doublets (Figure 8C). In the three-doublet fit, one doublet, contributing  $\sim 13\%$  of the total area, was constrained to have parameters obtained from the reference spectrum of the pure  $\text{Fe}_2(\text{III}/\text{III})$  state. The other two variable doublets, judged to originate from the paired  $\text{Fe}(\text{II})$  and  $\text{Fe}(\text{III})$  ions of a mixed-valent diiron cluster, were constrained to have equal areas. This fitting analysis yielded parameters of  $\delta_1 = 1.19 \text{ mm/s}$ ,  $\Delta E_{Q1} = 2.57 \text{ mm/s}$  for the high-spin  $\text{Fe}(\text{II})$  ion and  $\delta_2 = 0.52 \text{ mm/s}$ ,  $\Delta E_{Q2} = 0.96 \text{ mm/s}$  for the high-spin  $\text{Fe}(\text{III})$  ion of the coupled mixed-valent cluster and a total contribution of  $65\%$  of the original, experimental spectrum. The conclusion from this Mössbauer-spectroscopic analysis – that, upon treatment with an appropriately mild, one-electron reductant (ascorbate), the mixed-valent state of the diiron cluster accumulates to  $\sim 65\%$  in equilibrium with its fully reduced and fully oxidized forms – is consistent with the notion that TmpB is, like MIOX and PhnZ, an HD-MVDO.

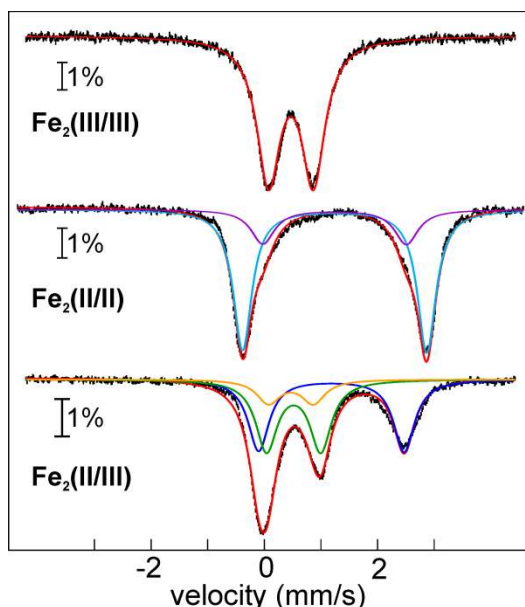
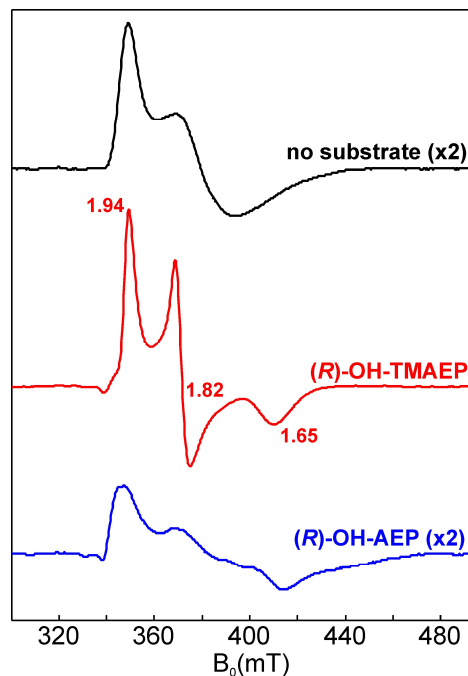


**Figure 8.** 120-K/0-T Mössbauer spectra of 2 mM  $\text{O}_2$ -free TmpA prepared in three oxidation states. All incubations were carried out for 45 min in an anoxic chamber. Experimental spectra

1  
2  
3 are shown as black vertical bars. Overall simulations are shown as red lines. (*Top*) Fe<sub>2</sub>(III/III)  
4 state obtained by treatment of the as-isolated protein with 3 mM potassium ferricyanide.  
5  
6 (*Middle*) Fe<sub>2</sub>(II/II) state obtained by treatment of the as-isolated protein with 20 mM sodium  
7  
8 dithionite. The two quadrupole-doublet components of the simulated spectrum of the Fe<sub>2</sub>(II/II)  
9  
10 complex are shown as purple and cyan lines; the parameters are provided in the main text.  
11  
12  
13 (*Bottom*) Fe<sub>2</sub>(II/III) state accumulated to ~ 65 % by treatment of the as-isolated protein with 20  
14  
15 mM sodium L-ascorbate. The simulated sub-spectra corresponding to the Fe<sub>2</sub>(II/III) species  
16  
17 (orange) and the paired Fe(II) (blue) and Fe(III) (green) sub-sites are shown as solid lines; their  
18  
19 parameters are provided in the main text. The contribution of the Fe<sub>2</sub>(II/II) species (22%) has  
20  
21 already been removed (by subtraction from the experimental spectrum; Figure S20) for clarity.  
22  
23  
24  
25  
26  
27  
28

29 Ascorbate-treated TmpB samples were also interrogated by EPR spectroscopy, both to  
30  
31 verify the oxidation state of the primary cofactor form inferred by Mössbauer spectroscopy and  
32  
33 to test for perturbations to the anticipated  $g < 2$  EPR signal upon substrate binding, as seen  
34  
35 previously for MIOX and PhnZ. In the absence of substrate (Figure 9, black), the sample  
36  
37 exhibited a broad axial signal with apparent principal  $g$ -values  $< 2$  [1.94, 1.78, 1.78]. This  
38  
39 spectrum is similar to those of antiferromagnetically-coupled ( $S_{\text{total}} = 1/2$ ) Fe<sub>2</sub>(II/III) clusters in  
40  
41 other proteins.<sup>21,79,80</sup> Comparison of the integrated intensity of this signal to that of a spin-  
42  
43 concentration Cu(II)-EDTA standard indicated the presence of ~ 0.3 spin/iron cluster or ~  
44  
45 0.6/diiron cluster, similar to the quantity deduced in the Mössbauer analysis of the parallel  
46  
47 sample. The signal became markedly more rhombic ( $g = [1.94, 1.82 \text{ and } 1.65]$ ) upon addition of  
48  
49 (*R*)-OH-TMAEP (Figure 9, red), suggestive of substrate binding to the cofactor, as also seen in  
50  
51 MIOX and PhnZ.<sup>21,79</sup> Addition of the unmethylated analog, (*R*)-OH-AEP (the PhnZ substrate),  
52  
53  
54  
55  
56  
57  
58  
59  
60

1  
2  
3 also perturbed the EPR spectrum but gave a broader, more complex signal (Figure 9, blue). The  
4  
5 spectrum in the presence of (*R*)-OH-AEP appears to be a superposition of more than one signal,  
6  
7 presumably representing bound and unbound states and/or multiple, conformationally distinct  
8  
9 forms of the (*R*)-OH-AEP complex.  
10  
11  
12  
13



14  
15  
16  
17  
18  
19  
20  
21  
22  
23  
24  
25  
26  
27  
28  
29  
30  
31  
32  
33  
34  
35  
36  
37 **Figure 9.** X-band EPR spectra of O<sub>2</sub>-free 0.25 mM TmpB after treatment with 10 mM sodium L-  
38 ascorbate (black) followed by addition of either 10 mM (*R*)-OH-TMAEP (red) or (*R*)-OH-AEP  
39 (blue). Experimental conditions: temperature = 10 K, microwave power = 0.2 mW, microwave  
40 frequency = 9.479 GHz, modulation amplitude = 1 mT.  
41  
42  
43  
44  
45  
46  
47

48 *TmpB*-catalyzed cleavage of the C–P bond in (*R*)-OH-TMAEP. With the EPR-spectroscopic data  
49 establishing that Fe<sub>2</sub>(II/III)-*TmpB* binds (*R*)-OH-TMAEP under anoxic conditions, we tested for  
50 consumption of the phosphonate compound in the presence of O<sub>2</sub>, anticipating that, by analogy  
51 to PhnZ, the C–P bond might be oxidatively cleaved to produce phosphate and the corresponding  
52  
53  
54  
55  
56  
57  
58  
59  
60

1  
2  
3 carboxylic acid [2-(trimethylammonio)acetate or glycine betaine]. Indeed, L-ascorbate-treated  
4 TmpB could consume > 200 equiv. of (*R*)-OH-TMAEP in the presence of sufficient O<sub>2</sub>, but no  
5  
6 conversion was observed under anoxic conditions (Figure 10A). The expected products of the  
7  
8 reaction were verified by LC-MS (for glycine betaine) and <sup>31</sup>P NMR (for phosphate) by  
9  
10 comparison to standards (Figure 10A). PhnZ, which natively acts on the corresponding  
11  
12 unmethylated analog, (*R*)-OH-AEP, could also oxidize (*R*)-OH-TMAEP to yield the same  
13  
14 products (Figure 10A). Conversely, TmpB consumed the PhnZ substrate, (*R*)-OH-AEP, very  
15  
16 inefficiently, promoting only five turnovers (to glycine and phosphate) in a 4-h incubation  
17  
18 (Figure 10B). This last result suggests that TmpB possesses some degree of preference for the *N*-  
19  
20 methylated substrates, as also shown above for TmpA. To explore this preference more  
21  
22 thoroughly, we challenged TmpB with the *N*-dimethyl analogue of its substrate, OH-DMAEP,  
23  
24 produced from DMEAP (presumably also with *R* configuration) by TmpA in a coupled reaction.  
25  
26 In this reaction, the expected products, phosphate and *N,N*-dimethylglycine, were readily  
27  
28 detected by <sup>31</sup>P-NMR and LC-MS, respectively, demonstrating that TmpB can indeed oxidize  
29  
30 OH-DMAEP (Figure S21). However, differences in the kinetics of the two hydroxylated  
31  
32 intermediates in the context of the coupled reaction again revealed the preference of TmpB for  
33  
34 the fully (tri)methylated substrate. Whereas (*R*)-OH-TMAEP accumulated transiently, OH-  
35  
36 DMAEP accumulation persisted throughout the reaction as a result of its slower consumption by  
37  
38 TmpB (Figure S21). This result demonstrates that TmpB prefers the substrate with the highest  
39  
40 degree of *N*-methylation, as also observed for TmpA.  
41  
42  
43  
44  
45  
46  
47  
48  
49  
50  
51  
52  
53  
54  
55  
56  
57  
58  
59  
60

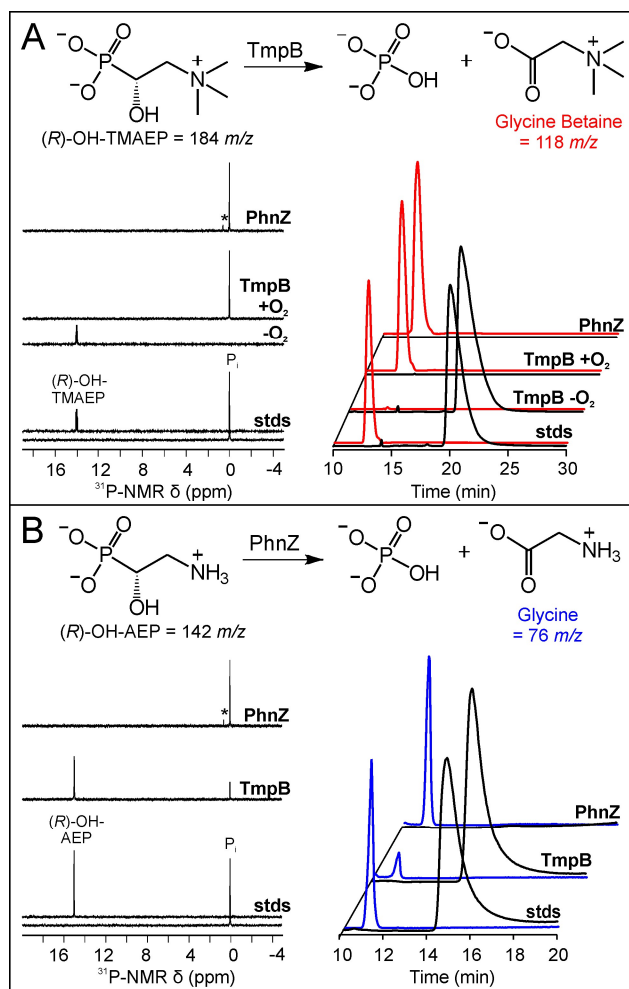


**Figure 10.** Activity of the HD-MVDOs against aminophosphonate compounds with and without *N*-methylation. The chemical transformations are depicted at the top of each panel. Aerobic reactions containing 0.01 mM TmpB or PhnZ, 0.2 mM L-ascorbate, and 2 mM of either (A) (*R*)-OH-TMAEP or (B) (*R*)-OH-AEP were incubated for 4 h at 3 °C. (*Left*) <sup>31</sup>P-NMR spectra detecting the substrates, (*R*)-OH-TMAEP or (*R*)-OH-AEP, and the product phosphate. The asterisks mark a contaminant present in the PhnZ protein preparation. (*Right*) LC-MS chromatograms detecting the substrates, (*R*)-OH-TMAEP or (*R*)-OH-AEP, and products, glycine betaine or glycine.



1  
2  
3 *Structural characterization of the TmpB•Fe<sub>2</sub>•(R)-OH-TMAEP complex.* The structure of diiron  
4 TmpB was solved by X-ray crystallography to a resolution of 1.63 Å. Phasing was achieved by  
5  
6 molecular replacement using the PhnZ structure (PDB accession code 4MLM)<sup>21</sup> as the search  
7  
8 model. The (R)-OH-TMAEP substrate was incorporated by soak methods; binding was observed  
9  
10 in two of the four monomers in the asymmetric unit (chains C and D). In the other two  
11  
12 monomers (chains A and B), lattice contacts that occlude the active site prevented substrate  
13  
14 binding in the crystal (Figure S22). The structure therefore provides two independent views of  
15  
16 the active site in the absence of substrate and two views of the enzyme•substrate complex. As  
17  
18 anticipated from the 32 % sequence identity, TmpB is structurally similar to PhnZ (Figure  
19  
20 S23),<sup>21,24</sup> with an rmsd of 1.5 Å for 181 C $\alpha$ -atoms.<sup>76</sup> The conserved fold is almost entirely  $\alpha$ -  
21  
22 helical (Figure 11A and Figure S23). Five core helices contribute the conserved histidine and  
23  
24 aspartate residues predicted from the extended HD-domain sequence motif (His40, His64,  
25  
26 Asp65, His86, His109, and Asp166 of *Lc* TmpB) to coordinate a dinuclear metal cofactor,  
27  
28 which was confirmed to be diiron by anomalous diffraction datasets collected at the Fe K-edge  
29  
30 (Figure 11B).  
31  
32  
33  
34  
35  
36  
37

38 In the substrate-free monomers, the active site cavity is quite solvent-exposed and the  
39  
40 first coordination sphere is completed by a (hydr)oxo bridge and two water ligands to iron site 2  
41  
42 (Fe2) (Figure 11B). In place of the water ligands in the other two monomers, clear electron  
43  
44 density for (R)-OH-TMAEP, continuous with the density arising from Fe2 (Figure 11C), is  
45  
46 observed. This direct coordination of the substrate to the cofactor rationalizes the associated  
47  
48 perturbations to its EPR spectrum. The (R)-OH-TMAEP molecule coordinates Fe2 in bidentate  
49  
50 fashion via its C1 hydroxyl group and a phosphonate oxygen (Figure 11C), the same substrate  
51  
52 binding mode previously observed in PhnZ.<sup>21,24</sup> The vicinal-diol substrate of MIOX (*myo*-  
53  
54  
55  
56  
57  
58  
59  
60

1  
2  
3 inositol) binds in a similar chelating mode to form a five-membered ring with Fe2 of the  
4 cofactor.<sup>25</sup> In all three cases, the scissile C–C/P bond is opposite the Fe ion in the five-membered  
5 ring. In the TmpB structure, the phosphonate dianion is further stabilized by salt bridges with the  
6 positively-charged side chains of Arg163 and Lys113, as well as hydrogen bonds with a water  
7 molecule and the side chains of Ser131, Ser134, and Gln138 (Figure S24). The interactions  
8 contributed by this phosphonate-binding pocket are fully conserved with those in the active site  
9 of PhnZ. The C1 hydroxyl group of the TmpB substrate hydrogen bonds with the imidazole side  
10 chain of conserved His68 (Figure S24) in the sequence motif (HDIGH) containing the metal-  
11 coordinated histidine-aspartate dyad. The combination of (i) this hydrogen-bonding motif, (ii)  
12 the bidentate substrate coordination of Fe2, and (iii) the *R* configuration of C1 orients the lone  
13 hydrogen of C1 toward Fe1, the proposed site of dioxygen activation.<sup>81</sup>

14  
15  
16  
17  
18  
19  
20  
21  
22  
23  
24  
25  
26  
27  
28  
29  
30  
31  
32  
33  
34  
35  
36  
37  
38  
39  
40  
41  
42  
43  
44  
45  
46  
47  
48  
49  
50  
51  
52  
53  
54  
55  
56  
57  
58  
59  
60

In all four active site views, Fe1 has an additional ligand (Figure 11), a tyrosine residue (Tyr30) that is conserved in all TmpB-like and PhnZ-like sequences. The corresponding tyrosine (Tyr24) was also seen to coordinate Fe1 in a structure of PhnZ lacking its substrate (Figure S23).<sup>24</sup> In both proteins, the Tyr ligand completes a nearly octahedral first coordination sphere of Fe1. Dioxygen binding is expected to be disfavored by this apparent coordinative saturation. In PhnZ, Tyr24 was observed not to coordinate in some structures of the PhnZ•Fe<sub>2</sub>•(*R*)-OH-AEP complex (Figure S23), suggesting that its transient dissociation upon substrate binding opens a site for O<sub>2</sub> addition/activation.<sup>24</sup> By contrast, in our structure of substrate-soaked TmpB, the Tyr30 ligand is retained, even in the monomers with substrate bound at Fe2. This inconsistency could be a consequence of introducing the substrate by soaking of pre-formed crystals, wherein established crystal contacts could disfavor Tyr30 dissociation. Alternatively, it could have resulted from a change in the cofactor oxidation state during crystallization to either of the non-

1  
2  
3 functional fully reduced or oxidized states. Regardless of the explanation for its failure to  
4 dissociate in the crystal, binding of (*R*)-OH-TMAEP by Fe<sub>2</sub>(II/III)-TmpB in solution results in  
5  
6 bleaching of a visible absorption feature at ~ 500 nm (Figure S25), which most likely arises from  
7  
8 the iron-tyrosinate interaction. This observation is consistent with the hypothesis that substrate-  
9  
10 promoted dissociation of the conserved tyrosine is functionally important in both phosphonate  
11  
12 cleaving HD-MVDOs.  
13  
14  
15

16  
17 In PhnZ, substrate triggered tyrosine dissociation was proposed to be driven by  
18  
19 interaction between the primary amine of (*R*)-OH-AEP and second-sphere Glu27, which is found  
20  
21 in an YxxE sequence motif adjacent to the Tyr24 ligand.<sup>24</sup> In substrate-free PhnZ, Glu27 residue  
22  
23 faces away from the active site (Figure S23). Conversely, in the substrate complex, both the  
24  
25 Glu27 side chain and the secondary structural motif in which it resides undergo a large  
26  
27 conformational change to position the Glu27 carboxylate for optimal interaction with the  
28  
29 substrate and to induce dissociation of Tyr24 (Figure S23). In TmpB, the corresponding  
30  
31 glutamate (Glu33) is held in place through an extensive hydrogen-bonding network in the active  
32  
33 site (Figures S23, S24), even in the absence of substrate, and appears unlikely to be capable of  
34  
35 the corresponding conformational change. The structure thus suggests that, if Tyr30 of TmpB  
36  
37 does indeed dissociate upon substrate binding, the structural mechanism driving the ligand  
38  
39 reorganization is likely to be distinct from that proposed for PhnZ.  
40  
41  
42  
43

44  
45 In both TmpB and PhnZ, the YxxE loop participates in multiple substrate binding  
46  
47 interactions. The carboxylate of the aforementioned Glu33 in TmpB is located ~3.3 Å from an  
48  
49 *N*-methyl group of the (*R*)-OH-TMAEP quaternary amine (Figures S23, S24). At this distance,  
50  
51 the carboxylate oxygen could be acting as an acceptor in a CH–O hydrogen-bonding interaction,  
52  
53 made possible by the partial positive charge on the carbon of this methyl group. In addition, the  
54  
55  
56  
57  
58  
59  
60

1  
2  
3 backbone amide oxygen of Leu31 is within 3.5 Å of another substrate *N*-methyl group, forming a  
4  
5 second CH–O interaction with (*R*)-OH-TMAEP (Figures S23, S24). In PhnZ, the corresponding  
6  
7 side chain and backbone functional groups also mediate enzyme-substrate contacts, but through  
8  
9 different intermolecular interactions. Glu27 interacts electrostatically with the (*R*)-OH-AEP  
10  
11 amine, and the backbone amide oxygen of Ile25 (corresponding to TmpB Leu31) hydrogen  
12  
13 bonds with what appears to be a functionally important water molecule (Figure S23). This water  
14  
15 molecule bridges an interaction between the substrate amine, the YxxE loop, and another flexible  
16  
17 loop that undergoes an open-to-closed transition that appears to sequester the active site from  
18  
19 solvent upon substrate binding (Figure S23).<sup>21,24</sup> The analogous loop (residues 69-84) in the  
20  
21 TmpB substrate-bound monomers remains disordered, resulting in a more exposed active site  
22  
23 (Figures 11A, Figure S23). Failure of TmpB to undergo full active site closure upon substrate  
24  
25 binding could again be attributed to the fact that the substrate was introduced by soaking of pre-  
26  
27 formed crystals. Inspection of the crystal lattice contacts near the residues 69-84 loop suggests  
28  
29 that the TmpB packing likely hinders this motion (Figure S22). The amino acid sequence of this  
30  
31 loop contains several aromatic and acidic residues (Figure S18), which could interact favorably  
32  
33 with the positively-charged quaternary amine of (*R*)-OH-TMAEP. However, there is no obvious  
34  
35 aromatic cage, analogous to the one seen in TmpA, to cradle the quaternary ammonium group.  
36  
37  
38  
39  
40  
41  
42  
43  
44  
45  
46  
47  
48  
49  
50  
51  
52  
53  
54  
55  
56  
57  
58  
59  
60

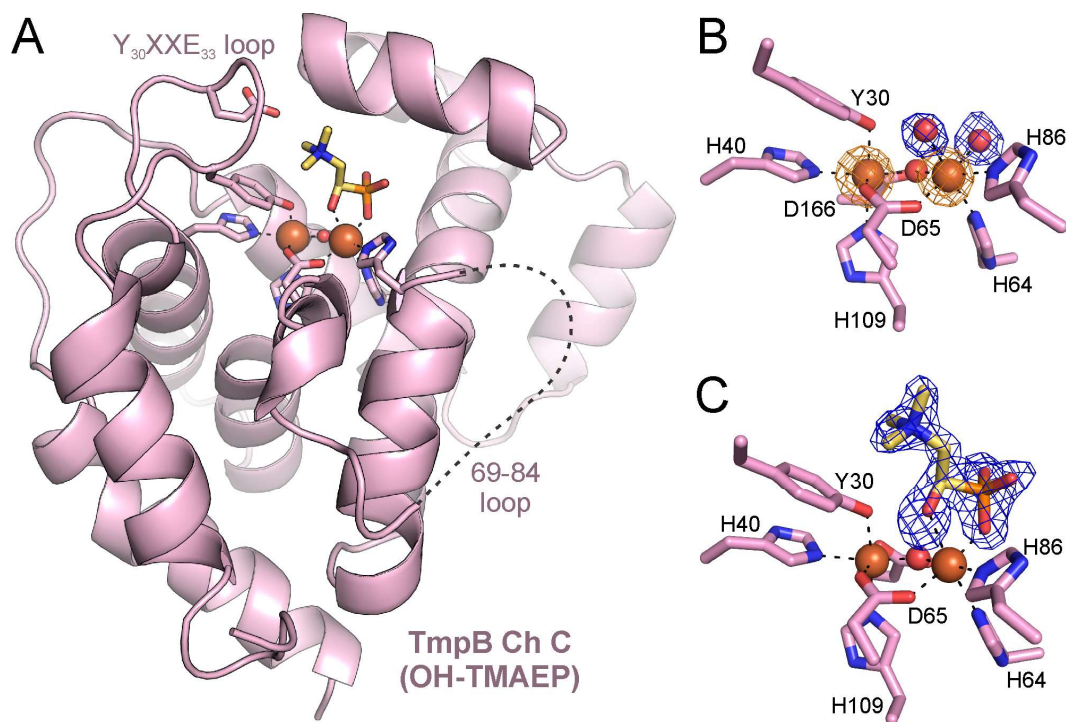


**Figure 11.** Views of TmpB from the X-ray crystal structure solved in this study. (A) Cartoon depiction of chain C of the TmpB structure. Iron ions are shown as brown spheres and (*R*)-OH-TMAEP (yellow) is shown in stick format. A dashed line represents the unmodeled region of the structure. TmpB active site of (B) chain A lacking substrate and (C) chain D with (*R*)-OH-TMAEP (yellow sticks) bound. Water molecules are shown as red spheres and iron ions as orange spheres. Orange mesh depicts the anomalous Fourier density contoured at  $10\sigma$ . Blue mesh depicts the  $F_o - F_c$  omit map contoured at  $3\sigma$  for either the coordinating water molecules or the substrate.

## DISCUSSION

Genomically co-located genes encoding presumptive TmpA and TmpB proteins have been identified in more than 350 bacterial genomes. Automated annotation correctly classified

1  
2  
3 these gene products into known structural superfamilies but failed to predict their biochemical  
4  
5 functions.  
6

7  
8 **Functional annotation of TmpA redefines substrate specificity.** The functional assignment of  
9  
10 TmpA as a  $\gamma$ -butyrobetaine hydroxylase posited both the type of reaction (hydroxylation) and the  
11  
12 primary substrate ( $\gamma$ bb); only the former assignment was correct. Our revised assignment of  
13  
14 TmpA as the first enzyme in a two-enzyme pathway to degrade the naturally occurring  
15  
16 phosphonate compound, TMAEP, is based on several observations. Among all compounds  
17  
18 screened, TMAEP was found to be the best substrate based on three metrics: binding, promotion  
19  
20 of O<sub>2</sub> activation (“substrate triggering”), and overall turnover efficiency. Whereas Fe/2OG  
21  
22 oxygenases often exhibit uncoupling of 2OG decarboxylation (to succinate) from oxidation of  
23  
24 non-native substrates, TmpA tightly couples succinate production with TMAEP hydroxylation.  
25  
26 TMAEP binding enhances the observed rate for reaction of the TmpA•Fe(II)•2OG cofactor with  
27  
28 dioxygen by more than 7,500-fold. Closely related compounds either do not promote O<sub>2</sub>  
29  
30 reactivity or do so to a lesser extent. O<sub>2</sub> activation in the presence of TMAEP leads to rapid  
31  
32 accumulation of the canonical hydrogen-abstracting ferryl intermediate<sup>14</sup> with an apparent  
33  
34 second-order rate constant of  $> 1.5 \times 10^6 \text{ M}^{-1} \cdot \text{s}^{-1}$  ( $k_{1,\text{obs}} \geq 750 \text{ s}^{-1}$ ,  $[\mathbf{R}] \sim 0.5 \text{ mM}$ ) at 5 °C, which  
35  
36 is, to the best of our knowledge, faster than any other Fe/2OG oxygenase for which this rate  
37  
38 constant has been reported.<sup>46,66,73,74</sup> Moreover, it is known that the substrate triggering efficacies  
39  
40 of native Fe/2OG-oxygenase substrates are generally greater than those of non-native  
41  
42 substrates,<sup>66</sup> as observed for TmpA with DMAEP. Thus, the remarkably fast reaction of the  
43  
44 TmpA•Fe(II)•2OG•TMAEP complex with O<sub>2</sub> is strong evidence that the *N*-  
45  
46 trimethyl/phosphonate compound is, in fact, the native substrate. The characteristic substrate  
47  
48 triggering in Fe/2OG enzymes is proposed to result, in part, from displacement of the axial water  
49  
50  
51  
52  
53  
54  
55  
56  
57  
58  
59  
60

1  
2  
3 ligand to open up a coordination site for O<sub>2</sub> binding.<sup>82,83</sup> In the structure of the  
4  
5 TmpA•Fe(II)•2OG•TMAEP complex, there is no density suggestive of an axial water, whereas  
6  
7 the water ligand is clearly present when only sulfate is bound in the primary substrate site. The  
8  
9 structural observations imply that the (potentially) general mechanism of substrate triggering –  
10  
11 axial water dissociation – is manifested upon binding of TMAEP to TmpA.  
12  
13

14  
15 TMAEP binding also induces structural changes beyond the first coordination sphere of  
16  
17 the metal center that likely enable reactivity and confer substrate specificity. The contraction of  
18  
19 the core β-barrel in the catalytic domain and closure of the lid loop positions substrate-interacting  
20  
21 residues into the active site. This closed lid-loop conformation is stabilized by its interaction with  
22  
23 the N-terminal domain of the opposite monomer, suggesting a role for the N-terminal domain in  
24  
25 both dimerization and substrate binding. Although the TmpA and BBOX N-terminal domains are  
26  
27 very similar, in terms of its secondary and tertiary structure, only BBOX harbors a Zn(II) ion in  
28  
29 its N-terminal domain. The Zn(II) ion is coordinated by a histidine residue and three cysteine  
30  
31 residues that are easily identified in the sequence by a CxCxxC motif.<sup>75</sup> Although the exact  
32  
33 function of this domain and the Zn(II) ion in BBOX is unknown, removal of the zinc abolishes  
34  
35 BBOX activity.<sup>84</sup> *Lc* TmpA does not possess this sequence motif, nor a Zn(II) metal in the  
36  
37 crystal structure, yet it maintains its structure. In conjunction with genomic context information,  
38  
39 the presence/absence of this Zn(II)-binding cysteine sequence motif could be used to  
40  
41 differentiate TmpA from BBOX function on the basis of primary structure. The potential for this  
42  
43 distinction to predict function of biochemically uncharacterized proteins is illustrated in the  
44  
45 analysis of bacterial genomes that contain multiple genes annotated as BBOXs (e.g., *Halomonas*  
46  
47 species). In the final SSN (Figure 2), the nodes representing the two proteins encoded within the  
48  
49 same *Halomonas* genome are separated into distinct clusters, already suggestive that they  
50  
51  
52  
53  
54  
55  
56  
57  
58  
59  
60

1  
2  
3 perform different functions. The protein that clusters with the known *Ps* BBOX is encoded  
4 within a putative  $\gamma$ bb degradation operon and possesses the Zn(II) binding motif (designated in  
5 the SSN by diamond nodes); it can thus be confidently assigned as a  $\gamma$ -butyrobetaine  
6 hydroxylase. Conversely, the protein that is clustered with *Lc* TmpA is encoded in an operon  
7 together with a TmpB-like HD domain protein and does not possess the Zn(II) binding sequence  
8 motif. We therefore suggest that it should be re-annotated as a TMAEP hydroxylase.  
9

10  
11  
12  
13  
14  
15  
16  
17 The occurrence of multiple genes annotated as BBOXs in a single genome indicates that  
18 BBOX and TmpA are likely paralogues, resulting from gene duplication and subsequent  
19 functional divergence. This relationship and common ancestry are evident both from their  
20 structural similarity and from the slight promiscuity of BBOX toward TMAEP. Unsurprisingly,  
21 their active sites are remarkably similar, particularly in the conserved set of aromatic residues  
22 that make cation- $\pi$  interactions with the positively-charged quaternary ammonium common to  
23 both substrates.<sup>85</sup> Aromatic cages are a classic structural feature of proteins that bind substrates  
24 with quaternary ammonium groups, such as acetylcholine esterases, phosphocholine-binding  
25 antibodies, acetylcholine receptors, epigenetic trimethyllysine reader domains, and  
26 trimethylamine dehydrogenases.<sup>78</sup> The cation- $\pi$  interaction is primarily electrostatic, with  
27 secondary contributions from hydrophobic interactions and desolvation, which imposes a  
28 requirement for a positively-charged functionality for efficient substrate recognition and  
29 binding.<sup>86,87</sup> This structurally-induced discrimination is obvious in the lack of TmpA activity  
30 toward phosphonates lacking any amine functionality. More subtly, TmpA even discriminates  
31 further on the basis of the degree of *N*-methylation, despite the fact that, at pH 7, the primary and  
32 tertiary amine groups of both 2-AEP and DMAEP should be protonated/cationic. Similar  
33 discrimination is observed for epigenetic methyllysine reader domains<sup>88,89</sup> and alkylamine  
34  
35  
36  
37  
38  
39  
40  
41  
42  
43  
44  
45  
46  
47  
48  
49  
50  
51  
52  
53  
54  
55  
56  
57  
58  
59  
60



1  
2  
3 dehydrogenases.<sup>78</sup> The reader domains that bind substrates with higher degrees of lysine *N*-  
4 methylation possess pockets with up to four aromatic residues, similar to that observed in TmpA.  
5  
6 Conversely, reader domains that recognize lower degrees of lysine *N*-methylation substitute one  
7  
8 or more of the aromatic residues with residues capable of hydrogen bonding with the extra  
9  
10 proton(s) on the amine. Furthermore, the *N*-methyl groups harbor some of the distributed  
11  
12 positive charge from the nitrogen,<sup>86</sup> perhaps enhancing the binding interaction and conferring the  
13  
14 observed specificity of TmpA for higher degrees of *N*-methylation.  
15  
16  
17  
18

19 The quaternary ammonium group is not, however, the sole basis for substrate  
20  
21 discrimination by TmpA, as the phosphonate functionality is also essential. It is also the major  
22  
23 distinguishing feature between the substrates of TmpA and BBOX. A simple but crucial  
24  
25 difference between the TmpA and BBOX active sites is the presence of Arg288 in TmpA, which  
26  
27 interacts electrostatically with the phosphonate moiety of TMAEP. Conversely, an alanine  
28  
29 residue is found at this position in *Hs* BBOX. A survey of reported substrate-bound structures of  
30  
31 enzymes that utilize phosphonate substrates reveals that there is almost invariably at least one  
32  
33 Arg that interacts with the phosphonate functional group (e.g., phosphonoacetaldehyde  
34  
35 dehydrogenase,<sup>90</sup> DhplI,<sup>91</sup> 2-AEP transaminase,<sup>92</sup> PhnZ,<sup>21,24</sup> and HppE<sup>93</sup>). This list now also  
36  
37 includes TmpB, which has a conserved arginine residue (Arg163) interacting with the  
38  
39 phosphonate moiety of (*R*)-OH-TMAEP. The specificity of TmpA for the phosphonate  
40  
41 functional group might suggest *a priori* that it would share structural homology and evolutionary  
42  
43 history with the organophosphonate hydroxylase, PhnY. Indeed, they enact identical chemical  
44  
45 transformations – hydroxylation of a carbon adjacent to a phosphonate – on substrates that differ  
46  
47 only in amine methylation. Yet TmpA and PhnY are only modestly similar in sequence, and  
48  
49  
50  
51  
52  
53  
54  
55  
56  
57  
58  
59  
60  
PhnY lacks the N-terminal domain common to both TmpA and BBOX. Instead, it is the

1  
2  
3 regioselectivity of hydroxylation with respect to the quaternary ammonium that is common to  
4  
5 TmpA and its homologue, BBOX. Thus, TmpA and PhnY likely evolved convergently to  
6  
7 promote similar reactions that initiate phosphonate degradation, to be completed by their HD-  
8  
9 MVDO partners.

10  
11  
12 **Functional annotation of TmpB redefines reaction and substrate specificity.** Conversely,  
13  
14 these partners, TmpB and PhnZ, likely share an evolutionary history that is reflected by their  
15  
16 cofactor, the chemical transformation they promote (oxidative C–P cleavage), and their structural  
17  
18 similarity. The x-ray crystallographic and spectroscopic (Mössbauer and EPR) data establish that  
19  
20 TmpB harbors a diiron cofactor. Importantly, the data show that TmpB shares with HD-MVDOs  
21  
22 the ability to stabilize the mixed-valent Fe<sub>2</sub>(II/III) oxidation state to as much as 60-70 % in  
23  
24 equilibrium with the more oxidized and reduced cofactor forms and to deploy this state as a  
25  
26 cofactor.<sup>21,23</sup> The longer-known ferritin-like diiron oxygenases react with dioxygen from the  
27  
28 Fe<sub>2</sub>(II/II) oxidation state and can typically accumulate the mixed-valent form to only modest  
29  
30 fractions (< 10 %).<sup>94-102</sup> Although the prediction of HD-MVDOs cannot rely solely on  
31  
32 identification of the extended sequence motif of metal ligands, the proteins that possess this  
33  
34 motif could serve as a pool to be mined for novel oxygenase functions. Thus, the metallocofactor  
35  
36 nuclearity should be considered in functional annotation of existing and newly identified HD-  
37  
38 domain proteins.

39  
40  
41 The substrate preference of TmpB for its *N*-trimethylated substrate mirrors the specificity  
42  
43 of TmpA. However, the structural basis for this discrimination by TmpB is not immediately  
44  
45 obvious from a simple comparison of its structure to that of PhnZ. The primary amine of (*R*-  
46  
47 OH-AEP forms a single contact with the PhnZ protein via the side chain of Glu27, which is also  
48  
49 conserved in TmpB (Glu33). The fact that the other interactions with the primary amine in PhnZ  
50  
51  
52  
53  
54  
55  
56  
57  
58  
59  
60

1  
2  
3 are mediated by water molecules may explain its greater substrate promiscuity. Conversely, the  
4 preference of TmpB for substrates with higher degrees of *N*-methylation is achieved by a more  
5 well-defined binding pocket mediated by direct protein contacts. In the structure of the  
6 TmpB•(*R*)-OH-TMAEP complex, the quaternary ammonium ion establishes CH–O hydrogen  
7 bonds<sup>103,104</sup> with the protein via its *N*-methyl groups, which harbor some positive charge.<sup>86</sup>  
8 Although there is more precedent for cation- $\pi$  interactions of quaternary-ammonium-containing  
9 substrates,<sup>78</sup> CH–O interactions have been observed in the binding pocket of the choline TMA-  
10 lyase enzyme CutC<sup>105</sup> and have been invoked in protein interactions with the sulfonium methyl  
11 group of *S*-adenosylmethionine.<sup>106</sup> In addition to these observed substrate contacts, the lid loop  
12 containing residues 69-84 in TmpB, which diverges greatly in sequence from that of PhnZ, likely  
13 plays a key role in substrate recognition. Unfortunately, due to the soaking method used to  
14 introduce the substrate and the obstructive crystal contacts, the lid loop remained disordered,  
15 preventing validation of this hypothesis.  
16  
17  
18  
19  
20  
21  
22  
23  
24  
25  
26  
27  
28  
29  
30  
31  
32

33 The observed substrate promiscuity of PhnZ for *N*-methylated substrates is not expected  
34 to be relevant in nature, because its partner hydroxylase, PhnY, is unable to convert the *N*-  
35 methylated substrate into the hydroxylated intermediate for PhnZ to utilize. Thus, for both the  
36 TmpA/B and the PhnY/Z pair, the specificity for degradation of the closely related phosphonate  
37 compounds is determined primarily by the Fe/2OG dioxygenase, rather than the HD-MVDO  
38 partner. Interestingly, we identified 16 cases in the sequence databases of a single operon  
39 possessing a single HD-domain protein but both BBOX-like and PhnY-like (PhyH-like) Fe/2OG  
40 oxygenases. While this type of operon could potentially represent a novel degradation pathway,  
41 it might also reflect the specialization of the Fe/2OG oxygenases and contrasting versatility of  
42 the HD-MVDOs. The Fe/2OG oxygenases could process different substrates, but the HD-  
43  
44  
45  
46  
47  
48  
49  
50  
51  
52  
53  
54  
55  
56  
57  
58  
59  
60

1  
2  
3 MVDO could degrade the products of both. The apparent dedication of the pathway partners – an  
4 Fe/2OG dioxygenase and an HD-MVDO – is also reflected by the co-occurrence of their  
5  
6 encoding genes in a single operon. In addition to the more than 300 examples of operons  
7  
8 containing separate genes for TmpA and TmpB, there are at least 59 examples of genes that  
9  
10 appear to encode fusions of TmpA and TmpB domains. There are also extant gene fusions of  
11  
12 PhnY and PhnZ. It is unknown whether these fusions fold to be functional two-domain enzymes,  
13  
14 but there is precedent for an active bifunctional protein with fused Fe/2OG oxygenase and  
15  
16 methyltransferase domains.<sup>107</sup> Nevertheless, the occurrence of the gene fusions supports the  
17  
18 notions that each pairing is specific and that the pair functions together.<sup>108</sup> Furthermore, the  
19  
20 frequent presence of a gene encoding a LysR-type transcriptional regulator upstream of the  
21  
22 TmpA/B genes suggests that they are co-transcribed and is consistent with the biochemical  
23  
24 evidence presented herein that their gene products constitute a degradation pathway. Similarly,  
25  
26 transcription of the operon encoding the PhnY/Z pair appears to be under control of a LysR-type  
27  
28 regulator. Transcriptional regulators of the LysR family<sup>109</sup> are commonly found upstream of  
29  
30 other known phosphonate degradation operons and, in some cases, have been shown to be  
31  
32 induced by the specific phosphonate compounds that the gene operon products catabolize.<sup>110-112</sup>  
33  
34 These precedents suggest that transcription of the appropriate degradation pair, TmpA/B or  
35  
36 PhnY/Z, would be specifically induced by the presence of TMAEP or 2-AEP, respectively.  
37  
38  
39

40  
41  
42 **Relevance of TmpA/B degradation pathway in microbes.** Phosphonates and their degradation  
43  
44 products serve valuable roles for the bacteria that occupy certain environmental niches.  
45  
46 Phosphonates exist in nature as components of phosphonolipids, phosphonoproteins, and  
47  
48 phosphonoglycans and are incorporated in the place of their phosphoester analogues, presumably  
49  
50 to confer the advantage of a more stable C–P bond in place of the hydrolyzable C–O–P bond.<sup>113-</sup>  
51  
52  
53  
54  
55  
56  
57  
58  
59  
60

1  
2  
3 115 Of the most common phosphoesters, phosphoethanolamine, phosphoserine, and  
4 phosphocholine, each has a phosphonate counterpart (2-AEP, phosphonoalanine, and TMAEP,  
5 respectively). While 2-AEP is the most abundant phosphonate in nature, TMAEP, as well as  
6 DMAEP and *N*-methyl-AEP, have been reported in protozoa and marine invertebrates such as  
7 sea anemones, marine plankton, and algae.<sup>114,116-118</sup> Degradation pathways for both 2-AEP and  
8 phosphonoalanine have been discovered, ultimately producing phosphate and a source of  
9 carbon.<sup>119-123</sup> The TmpA/B pathway mirrors the PhnY/Z degradation pathway for 2-AEP in its  
10 chemical transformations but is instead specific for TMAEP. It represents the first example of a  
11 pathway for microbial metabolism of this naturally occurring phosphonate compound.  
12  
13  
14  
15  
16  
17  
18  
19  
20  
21  
22  
23

24 The TmpA/B operon is found primarily in Proteobacteria and Actinobacteria, with  
25 considerable representation in marine and N<sub>2</sub>-fixing plant-symbiotic bacteria. The products of  
26 this degradation pathway, phosphate and glycine betaine, are valuable nutrients for such bacteria.  
27 Organophosphonates have been established as major sources of phosphorus in marine  
28 environments, which are limited in this essential nutrient.<sup>119</sup> Phosphorus has been found to  
29 enhance plant growth, promote formation of crucial root nodules where the symbiotic bacteria  
30 reside, and support higher levels of N<sub>2</sub>-fixation by the symbiotes.<sup>124-128</sup> Many bacteria possess  
31 multiple phosphonate degradation pathways to extract phosphate, but the requirement for  
32 different specialized pathways and their cooperation are poorly understood.<sup>119-122</sup> Nevertheless,  
33 the ubiquity of mechanisms for the release of phosphate from dissolved organic phosphorus  
34 sources highlights their necessity and utility. The second product of the TmpA/B pathway,  
35 glycine betaine, is a known osmoprotectant. In marine bacteria, osmoregulation by compounds  
36 with quaternary ammonium functionality is common to protect against high salinity.<sup>129</sup> Glycine  
37 betaine is the most potent osmoprotectant in some N<sub>2</sub>-fixing bacteria, enhancing their growth  
38  
39  
40  
41  
42  
43  
44  
45  
46  
47  
48  
49  
50  
51  
52  
53  
54  
55  
56  
57  
58  
59  
60

1  
2  
3 under conditions of osmotic stress,<sup>131,132</sup> which diminishes their ability to fix nitrogen.<sup>130,131,132</sup>  
4  
5 Glycine betaine can also be utilized as a source of carbon and nitrogen upon its demethylation to  
6  
7 glycine.<sup>133-135</sup> Degradation of TMEAP for nutrients could provide a competitive advantage for  
8  
9 soil bacteria,<sup>134</sup> particularly for colonization of the environmental niche of plant roots.  
10  
11  
12  
13

## 14 CONCLUSIONS

15  
16 We have defined the biochemical reactions of the Fe/2OG oxygenase, TmpA, and the  
17  
18 HD-domain protein, TmpB, to elucidate a new pathway for degradation of the natural  
19  
20 organophosphonate, TMAEP. The combination of genomic context and structure-informed  
21  
22 sequence motifs will allow for the proper identification and annotation of the genes associated  
23  
24 with this pathway in existing and newly sequenced genomes. More broadly, the biochemical and  
25  
26 structural information gleaned about these subsets of proteins could potentially inform  
27  
28 bioinformatic analyses aiming to categorize and predict functions within their large  
29  
30 superfamilies.  
31  
32  
33  
34  
35  
36  
37

## 38 ACCESSION CODES

39  
40 *Lc* TmpA: NCBI RefSeq WP\_027237574.1

41  
42 PDB 6NPB, 6NPC, 6NPD

43  
44 *Lc* TmpB: NCBI RefSeq WP\_027237573.1

45  
46 PDB 6NPA  
47  
48  
49  
50

51 **ACKNOWLEDGMENTS** The authors thank Prof. Christopher J. Schofield (University of  
52  
53 Oxford, UK) for the library of betaine compounds and *Ps* BBOX plasmid, Prof. Wilfred A. van  
54  
55  
56  
57

1  
2  
3 der Donk (University of Illinois, Urbana-Champaign) for the library of phosphonate compounds,  
4  
5 the Shared Fermentation Facility of The Pennsylvania State University (University Park, PA) for  
6  
7 use of the Microfluidics M-110EH-30 microfluidizer processor, Mr. Henry Gong at the  
8  
9 Pennsylvania State Materials Research Institute (University Park, PA) for ICP-AES analysis, and  
10  
11 Dr. Emmanuel Hatzakis at the Pennsylvania State University Nuclear Magnetic Resonance  
12  
13 facility.  
14  
15  
16  
17  
18

### 19 SUPPORTING INFORMATION AVAILABLE

20  
21 The Supporting Information includes procedures for protein purification and substrate synthesis,  
22  
23 tables S1-2 reporting crystallographic data collection, tables S3-4, and figures S1-S25. It can be  
24  
25 obtained online free of charge.  
26  
27  
28  
29

### 30 REFERENCES

- 31  
32  
33 [1] Sono, M., Roach, M. P., Coulter, E. D., Dawson, J. H. (1996) Heme-containing oxygenases.  
34 *Chem. Rev.* 96, 2841-2888.  
35 [2] Hausinger, R. P. (2015) *2-Oxoglutarate-Dependent Oxygenases*, Hausinger, R. P., Schofield  
36 C. J., Ed., The Royal Society of Chemistry.  
37 [3] Andrews, S. C. (2010) The ferritin-like superfamily: Evolution of the biological iron  
38 storeman from a rubrerythrin-like ancestor. *Biochim. Biophys. Acta.* 1800, 691-705.  
39 [4] Aravind, L., Koonin, E. V. (1998) The HD domain defines a new superfamily of metal-  
40 dependent phosphohydrolases. *Trends Biochem. Sci.* 23, 469-472.  
41 [5] Baier, F., Copp, J. N., Tokuriki, N. (2016) Evolution of enzyme superfamilies:  
42 Comprehensive exploration of sequence-function relationships. *Biochemistry* 55, 6375-  
43 6388.  
44 [6] Roche, D. B., Bruls, T. (2015) The enzymatic nature of an anonymous protein sequence  
45 cannot reliably be inferred from superfamily level structural information alone. *Protein*  
46 *Sci.* 24, 643-650.  
47 [7] Galperin, M. Y., Koonin, E. V. (2012) Divergence and convergence in enzyme evolution. *J.*  
48 *Biol. Chem.* 287, 21-28.  
49 [8] Gaudet, P., Livstone, M. S., Lewis, S. E., Thomas, P. D. (2011) Phylogenetic-based  
50 propagation of functional annotations within the Gene Ontology consortium. *Brief.*  
51 *Bioinform.* 12, 449-462.  
52  
53  
54  
55  
56  
57  
58  
59  
60

- 1  
2  
3 [9] du Plessis, L., Skunca, N., Dessimoz, C. (2011) The what, where, how and why of gene  
4 ontology--a primer for bioinformaticians. *Brief Bioinform.* 12, 723-735.
- 5 [10] Skunca, N., Altenhoff, A., Dessimoz, C. (2012) Quality of computationally inferred gene  
6 ontology annotations. *PLoS Comput. Biol.* 8, e1002533.
- 7 [11] Aik, W., McDonough, M. A., Thalhammer, A., Chowdhury, R., Schofield, C. J. (2012) Role  
8 of the jelly-roll fold in substrate binding by 2-oxoglutarate oxygenases. *Curr. Opin.*  
9 *Struct. Biol.* 22, 691-700.
- 10 [12] Koehntop, K. D., Emerson, J. P., Que, L., Jr. (2005) The 2-His-1-carboxylate facial triad: a  
11 versatile platform for dioxygen activation by mononuclear non-heme iron(II) enzymes. *J.*  
12 *Biol. Inorg. Chem.* 10, 87-93.
- 13 [13] Hegg, E. L., Que, L., Jr. (1997) The 2-His-1-carboxylate facial triad - An emerging  
14 structural motif in mononuclear non-heme iron(II) enzymes. *Eur. J. Biochem.* 250, 625-  
15 629.
- 16 [14] Price, J. C., Barr, E. W., Tirupati, B., Bollinger, J. M., Jr., Krebs, C. (2003) The first direct  
17 characterization of a high-valent iron intermediate in the reaction of an alpha-  
18 ketoglutarate-dependent dioxygenase: A high-spin Fe(IV) complex in taurine/alpha-  
19 ketoglutarate dioxygenase (TauD) from *Escherichia coli*. *Biochemistry* 42, 7497-7508.
- 20 [15] Bollinger, J. M., Jr., Chang, W.-c., Matthews, M. L., Martinie, R. J., Boal, A. K., Krebs, C.  
21 (2015) Mechanisms of 2-oxoglutarate-dependent oxygenases: The hydroxylation  
22 paradigm and beyond, In *2-Oxoglutarate-dependent oxygenases*, pp 95-122, The Royal  
23 Society of Chemistry.
- 24 [16] Murray, K. D., Bremer, H. (1996) Control of spoT-dependent ppGpp synthesis and  
25 degradation in *Escherichia coli*. *J. Mol. Biol.* 259, 41-57.
- 26 [17] Francis, S. H., Colbran, J. L., McAllister-Lucas, L. M., Corbin, J. D. (1994) Zinc  
27 interactions and conserved motifs of the cGMP-binding cGMP-specific  
28 phosphodiesterase suggest that it is a zinc hydrolase. *J. Biol. Chem.* 269, 22477-22480.
- 29 [18] Johnson, G. S., Adler, C. R., Collins, J. J., Court, D. (1979) Role of the spoT gene product  
30 and manganese ion in the metabolism of guanosine 5'-diphosphate 3'-diphosphate in  
31 *Escherichia coli*. *J. Biol. Chem.* 254, 5483-5487.
- 32 [19] Quirk, S., Bessman, M. J. (1991) dGTP triphosphohydrolase, a unique enzyme confined to  
33 members of the family *Enterobacteriaceae*. *J. Bacteriol.* 173, 6665-6669.
- 34 [20] Bollinger, J. M., Jr., Diao, Y., Matthews, M. L., Xing, G., Krebs, C. (2009) *myo*-Inositol  
35 oxygenase: a radical new pathway for O(2) and C-H activation at a nonheme diiron  
36 cluster. *Dalton Trans.*, 905-914.
- 37 [21] Wörsdörfer, B., Lingaraju, M., Yennawar, N. H., Boal, A. K., Krebs, C., Bollinger, J. M.,  
38 Jr., Pandelia, M.-E. (2013) Organophosphonate-degrading PhnZ reveals an emerging  
39 family of HD domain mixed-valent diiron oxygenases. *Proc. Natl. Acad. Sci. U S A* 110,  
40 18874-18879.
- 41 [22] McSorley, F. R., Wyatt, P. B., Martinez, A., DeLong, E. F., Hove-Jensen, B., Zechel, D. L.  
42 (2012) PhnY and PhnZ comprise a new oxidative pathway for enzymatic cleavage of a  
43 carbon-phosphorus bond. *J. Am. Chem. Soc.* 134, 8364-8367.
- 44 [23] Xing, G., Barr, E. W., Diao, Y., Hoffart, L. M., Prabhu, K. S., Arner, R. J., Reddy, C. C.,  
45 Krebs, C., Bollinger, J. M., Jr. (2006) Oxygen activation by a mixed-valent, diiron(II/III)  
46 cluster in the glycol cleavage reaction catalyzed by *myo*-inositol oxygenase. *Biochemistry*  
47 45, 5402-5412.
- 48  
49  
50  
51  
52  
53  
54  
55  
56  
57  
58  
59  
60



- 1  
2  
3 [24] van Staalduinen, L. M., McSorley, F. R., Schiessl, K., Seguin, J., Wyatt, P. B.,  
4 Hammerschmidt, F., Zechel, D. L., Jia, Z. (2014) Crystal structure of PhnZ in complex  
5 with substrate reveals a di-iron oxygenase mechanism for catabolism of  
6 organophosphonates. *Proc. Natl. Acad. Sci. U S A* *111*, 5171-5176.
- 7  
8 [25] Brown, P. M., Caradoc-Davies, T. T., Dickson, J. M., Cooper, G. J., Loomes, K. M., Baker,  
9 E. N. (2006) Crystal structure of a substrate complex of *myo*-inositol oxygenase, a di-iron  
10 oxygenase with a key role in inositol metabolism. *Proc. Natl. Acad. Sci. U S A* *103*,  
11 15032-15037.
- 12  
13 [26] Lovering, A. L., Capeness, M. J., Lambert, C., Hopley, L., Sockett, R. E. (2011) The  
14 structure of an unconventional HD-GYP protein from *Bdellovibrio* reveals the roles of  
15 conserved residues in this class of cyclic-di-GMP phosphodiesterases. *mBio* *2*, e00163-  
16 00111.
- 17  
18 [27] Benda, C., Ebert, J., Scheltema, R. A., Schiller, H. B., Baumgartner, M., Bonneau, F.,  
19 Mann, M., Conti, E. (2014) Structural model of a CRISPR RNA-silencing complex  
20 reveals the RNA-target cleavage activity in Cmr4. *Mol. Cell* *56*, 43-54.
- 21  
22 [28] Jung, T. Y., An, Y., Park, K. H., Lee, M. H., Oh, B. H., Woo, E. (2015) Crystal structure of  
23 the Csm1 subunit of the Csm complex and its single-stranded DNA-specific nuclease  
24 activity. *Structure* *23*, 782-790.
- 25  
26 [29] Gerlt, J. A., Allen, K. N., Almo, S. C., Armstrong, R. N., Babbitt, P. C., Cronan, J. E.,  
27 Dunaway-Mariano, D., Imker, H. J., Jacobson, M. P., Minor, W., Poulter, C. D., Raushel,  
28 F. M., Sali, A., Shoichet, B. K., Sweedler, J. V. (2011) The Enzyme Function Initiative.  
29 *Biochemistry* *50*, 9950-9962.
- 30  
31 [30] Peng, J., Uygun, S., Kim, T., Wang, Y., Rhee, S. Y., Chen, J. (2015) Measuring semantic  
32 similarities by combining gene ontology annotations and gene co-function networks.  
33 *BMC Bioinform.* *16*.
- 34  
35 [31] Sjölander, K., Datta, R. S., Shen, Y., Shoffner, G. M. (2011) Ortholog identification in the  
36 presence of domain architecture rearrangement. *Brief. Bioinform.* *12*, 413-422.
- 37  
38 [32] Teng, Z., Guo, M., Liu, X., Dai, Q., Wang, C., Xuan, P. (2013) Measuring gene functional  
39 similarity based on group-wise comparison of GO terms. *Bioinformatics* *29*, 1424-1432.
- 40  
41 [33] Wolf, Y. I., Rogozin, I. B., Kondrashov, A. S., Koonin, E. V. (2001) Genome alignment,  
42 evolution of prokaryotic genome organization, and prediction of gene function using  
43 genomic context. *Genome Res.* *11*, 356-372.
- 44  
45 [34] Korbel, J. O., Jensen, L. J., von Mering, C., Bork, P. (2004) Analysis of genomic context:  
46 prediction of functional associations from conserved bidirectionally transcribed gene  
47 pairs. *Nat. Biotechnol.* *22*, 911-917.
- 48  
49 [35] Rogozin, I. B., Makarova, K. S., Murvai, J., Czabarka, E., Wolf, Y. I., Tatusov, R. L.,  
50 Szekely, L. A., Koonin, E. V. (2002) Connected gene neighborhoods in prokaryotic  
51 genomes. *Nucleic Acids Res.* *30*, 2212-2223.
- 52  
53 [36] Gabaldon, T., Huynen, M. A. (2004) Prediction of protein function and pathways in the  
54 genome era. *Cell. Mol. Life Sci.* *61*, 930-944.
- 55  
56 [37] Huynen, M., Snel, B., Lath, W. I., Bork, P. (2000) Exploitation of gene context. *Curr. Op.*  
57 *Struct. Biol.* *10*, 366-370.
- 58  
59 [38] Bremer, J. (1983) Carnitine--metabolism and functions. *Physiol. Rev.* *63*, 1420-1480.
- 60 [39] Lindstedt, G., Lindstedt, S., Midtvedt, T., Tofft, M. (1970) Inducible gamma-butyrobetaine-  
degrading enzymes in *Pseudomonas* species AK 1. *J. Bacteriol.* *101*, 1094-1095.

- 1  
2  
3 [40] Rebouche, C. J., Seim, H. (1998) Carnitine metabolism and its regulation in microorganisms  
4 and mammals. *Annu. Rev. Nutr.* 18, 39-61.
- 5 [41] Vandecandelaere, I., Segaeert, E., Mollica, A., Faimali, M., Vandamme, P. (2008) *Leisingera*  
6 *aquimarina* sp. nov., isolated from a marine electroactive biofilm, and emended  
7 descriptions of *Leisingera methylohalidivorans* Schaefer et al. 2002, *Phaeobacter*  
8 *daeponensis* Yoon et al. 2007 and *Phaeobacter inhibens* Martens et al. 2006. *Int. J. Syst.*  
9 *Evol. Microbiol.* 58, 2788-2793.
- 10 [42] Breider, S., Scheuner, C., Schumann, P., Fiebig, A., Petersen, J., Pradella, S., Klenk, H. P.,  
11 Brinkhoff, T., Goker, M. (2014) Genome-scale data suggest reclassifications in the  
12 *Leisingera-Phaeobacter* cluster including proposals for *Sedimentitalea* gen. nov. and  
13 *Pseudophaeobacter* gen. nov. *Front. Microbiol.* 5, 416.
- 14 [43] Gerlt, J. A., Bouvier, J. T., Davidson, D. B., Imker, H. J., Sadkhin, B., Slater, D. R.,  
15 Whalen, K. L. (2015) Enzyme Function Initiative-Enzyme Similarity Tool (EFI-EST): A  
16 web tool for generating protein sequence similarity networks. *BBA-Proteins Proteom.*  
17 1854, 1019-1037.
- 18 [44] Shannon, P., Markiel, A., Ozier, O., Baliga, N. S., Wang, J. T., Ramage, D., Amin, N.,  
19 Schwikowski, B., Ideker, T. (2003) Cytoscape: A software environment for integrated  
20 models of biomolecular interaction networks. *Genome Res.* 13, 2498-2504.
- 21 [45] Markowitz, V. M., Chen, I. M. A., Palaniappan, K., Chu, K., Szeto, E., Grechkin, Y.,  
22 Ratner, A., Jacob, B., Huang, J. H., Williams, P., Huntemann, M., Anderson, I.,  
23 Mavromatis, K., Ivanova, N. N., Kyrpides, N. C. (2012) IMG: the integrated microbial  
24 genomes database and comparative analysis system. *Nucleic Acids Res.* 40, D115-D122.
- 25 [46] Price, J. C., Barr, E. W., Hoffart, L. M., Krebs, C., Bollinger J. M., J. (2005) Kinetic  
26 dissection of the catalytic mechanism of taurine: $\alpha$ -ketoglutarate dioxygenase (TauD)  
27 from *Escherichia coli*. *Biochemistry* 44, 8138-8147.
- 28 [47] Otwinowski, Z., Minor, W. (1997) Processing of X-ray diffraction data collected in  
29 oscillation mode. *Method. Enzymol.* 276, 307-326.
- 30 [48] Murshudov, G. N., Skubak, P., Lebedev, A. A., Pannu, N. S., Steiner, R. A., Nicholls, R. A.,  
31 Winn, M. D., Long, F., Vagin, A. A. (2011) REFMAC5 for the refinement of  
32 macromolecular crystal structures. *Acta. Crystallogr. D Biol. Crystallogr.* 67, 355-367.
- 33 [49] Emsley, P., Lohkamp, B., Scott, W. G., Cowtan, K. (2010) Features and development of  
34 Coot. *Acta. Crystallogr. D Biol. Crystallogr.* 66, 486-501.
- 35 [50] Chen, V. B., Arendall, W. B., Headd, J. J., Keedy, D. A., Immormino, R. M., Kapral, G. J.,  
36 Murray, L. W., Richardson, J. S., Richardson, D. C. (2010) MolProbity: all-atom  
37 structure validation for macromolecular crystallography. *Acta. Crystallogr. D Biol.*  
38 *Crystallogr.* 66, 12-21.
- 39 [51] McCoy, A. J., Grosse-Kunstleve, R. W., Adams, P. D., Winn, M. D., Storoni, L. C., Read,  
40 R. J. (2007) Phaser crystallographic software. *J. Appl. Crystallogr.* 40, 658-674.
- 41 [52] Langer, G. G., Hazledine, S., Wiegels, T., Carolan, C., Lamzin, V. S. (2013) Visual  
42 automated macromolecular model building. *Acta. Crystallogr. D Biol. Crystallogr.* 69,  
43 635-641.
- 44 [53] Lebedev, A. A., Young, P., Isupov, M. N., Moroz, O. V., Vagin, A. A., Murshudov, G. N.  
45 (2012) JLigand: a graphical tool for the CCP4 template-restraint library. *Acta.*  
46 *Crystallogr. D Biol. Crystallogr.* 68, 431-440.
- 47 [54] Vagin, A., Teplyakov, A. (1997) MOLREP: an automated program for molecular  
48 replacement. *J. Appl. Crystallogr.* 30, 1022-1025.
- 49  
50  
51  
52  
53  
54  
55  
56  
57  
58  
59  
60

- 1  
2  
3 [55] The 4.2 K/53 mT spectrum also shows broad baseline features in addition to the quadrupole  
4 doublet, suggesting the presence of a mononuclear high spin ferric ( $S = 5/2$ ) species. This  
5 minority species, which is also detected by EPR spectroscopy with an effective g-value of  
6  $\sim 4.3$ , is attributed to adventitiously-bound iron observed in the x-ray crystal structure,  
7 rather than partial occupancy of the diiron cofactor (Figure S19)  
8  
9 [56] Immirzi, A. (1966), Ahmed, F. R., Ed., Munksgaard.  
10 [57] Ten Eyck, L. F. (1973) Crystallographic Fast Fourier Transforms. *Acta Cryst. A29*, 183-191.  
11 [58] Read, R. J., Schierbeek, A. J. (1988) A phased translation function. *J. Appl. Cryst. 21*, 490-  
12 495.  
13 [59] Winn, M. D., Ballard, C. C., Cowtan, K. D., Dodson, E. J., Emsley, P., Evans, P. R.,  
14 Keegan, R. M., Krissinel, E. B., Leslie, A. G., McCoy, A., McNicholas, S. J.,  
15 Murshudov, G. N., Pannu, N. S., Potterton, E. A., Powell, H. R., Read, R. J., Vagin, A.,  
16 Wilson, K. S. (2011) Overview of the CCP4 suite and current developments. *Acta*  
17 *Crystallogr. D Biol. Crystallogr. 67*, 235-242.  
18 [60] Lindstedt, G., Lindstedt, S., Midtvedt, T., Tofft, M. (1967) Hydroxylation of gamma-  
19 butyrobetaine to carnitine. *Biochem. J. 103*, 1271-1282.  
20 [61] Lindstedt, G., Lindstedt, S., Olander, B., Tofft, M. (1968) Alpha-ketoglutarate and  
21 hydroxylation of gamma-butyrobetaine. *Biochim. Biophys. Acta. 158*, 503-505.  
22 [62] Lindstedt, G., Lindstedt, S., Nordin, I. (1977) Purification and Properties of Gamma-  
23 Butyrobetaine Hydroxylase from *Pseudomonas-Sp-Ak-1*. *Biochemistry 16*, 2181-2188.  
24 [63] Atkinson, H. J., Morris, J. H., Ferrin, T. E., Babbitt, P. C. (2009) Using Sequence Similarity  
25 Networks for visualization of relationships across diverse protein superfamilies. *PLoS*  
26 *One 4*, e4345.  
27 [64] Kazaks, A., Makrecka-Kuka, M., Kuka, J., Voronkova, T., Akopjana, I., Grinberga, S.,  
28 Pugovics, O., Tars, K. (2014) Expression and purification of active, stabilized  
29 trimethyllysine hydroxylase. *Protein Expr. Purif. 104*, 1-6.  
30 [65] Pavel, E. G., Zhou, J., Busby, R. W., Gunsior, M., Townsend, C. A., Solomon, E. I. (1998)  
31 Circular dichroism and magnetic circular dichroism spectroscopic studies of the non-  
32 heme ferrous active site in clavaminic synthase and its interaction with alpha-  
33 ketoglutarate cosubstrate. *J. Am. Chem. Soc. 120*, 743-753.  
34 [66] Matthews, M. L., Krest, C. M., Barr, E. W., Vaillancourt, F. H., Walsh, C. T., Green, M. T.,  
35 Krebs, C., Bollinger, J. M., Jr. (2009) Substrate-triggered formation and remarkable  
36 stability of the C-H bond-cleaving chloroferryl intermediate in the aliphatic halogenase,  
37 SyrB2. *Biochemistry 48*, 4331-4343.  
38 [67] Ryle, M. J., Padmakumar, R., Hausinger, R. P. (1999) Stopped-flow kinetic analysis of  
39 *Escherichia coli* taurine/alpha-ketoglutarate dioxygenase: Interactions with alpha-  
40 ketoglutarate, taurine, and oxygen. *Biochemistry 38*, 15278-15286.  
41 [68] Solomon, E. I., Brunold, T. C., Davis, M. I., Kemsley, J. N., Lee, S. K., Lehnert, N., Neese,  
42 F., Skulan, A. J., Yang, Y. S., Zhou, J. (2000) Geometric and electronic  
43 structure/function correlations in non-heme iron enzymes. *Chem. Rev. 100*, 235-349.  
44 [69] Decker, A., Clay, M. D., Solomon, E. I. (2006) Spectroscopy and electronic structures of  
45 mono- and binuclear high-valent non-heme iron-oxo systems. *J. Inorg. Biochem 100*,  
46 697-706.  
47 [70] Krebs, C., Fujimori, D. G., Walsh, C. T., Bollinger, J. M., Jr. (2007) Non-heme Fe(IV)-oxo  
48 intermediates. *Acc. Chem. Res. 40*, 484-492.  
49  
50  
51  
52  
53  
54  
55  
56  
57  
58  
59  
60

- 1  
2  
3 [71] Hoffart, L. M., Barr, E. W., Guyer, R. B., Bollinger Jr, J. M., Krebs, C. (2006) Direct  
4 spectroscopic detection of a C-H-cleaving high-spin Fe(IV) complex in a prolyl-4-  
5 hydroxylase. *Proc. Natl. Acad. Sci. U S A* 103, 14738-14743.
- 6  
7 [72] Pan, J., Bhardwaj, M., Zhang, B., Chang, W.-c., Schardl, C. L., Krebs, C., Grossman, R. B.,  
8 Bollinger, J. M., Jr. (2018) Installation of the ether bridge of lolines by the iron- and 2-  
9 oxoglutarate-dependent oxygenase, LolO: Regio- and stereochemistry of sequential  
10 hydroxylation and oxacyclization reactions. *Biochemistry* 57, 2074-2083.
- 11 [73] Dunham, N. P., Chang, W.-c., Mitchell, A. J., Martinie, R. J., Zhang, B., Bergman, J. A.,  
12 Rajakovich, L. J., Wang, B., Silakov, A., Krebs, C., Boal, A. K., Bollinger, J. M., Jr.  
13 (2018) Two distinct mechanisms for C-C desaturation by iron(II)- and 2-(oxo)glutarate-  
14 dependent oxygenases: Importance of alpha-heteroatom assistance. *J. Am. Chem. Soc.*  
15 *140*, 7116-7126.
- 16  
17 [74] Dunham, N. P., Mitchell, A. J., Del Rio Pantoja, J. M., Krebs, C., Bollinger, J. M., Jr., Boal,  
18 A. K. (2018)  $\alpha$ -Amine desaturation of d-arginine by the iron(II)- and 2-(oxo)glutarate-  
19 dependent l-arginine 3-hydroxylase, VioC. *Biochemistry* 57, 6479-6488.
- 20 [75] Leung, I. K., Krojer, T. J., Kochan, G. T., Henry, L., von Delft, F., Claridge, T. D.,  
21 Oppermann, U., McDonough, M. A., Schofield, C. J. (2010) Structural and mechanistic  
22 studies on gamma-butyrobetaine hydroxylase. *Chem. Biol.* 17, 1316-1324.
- 23 [76] Krissinel, E., Henrick, K. (2004) Secondary-structure matching (SSM), a new tool for fast  
24 protein structure alignment in three dimensions. *Acta. Crystallogr. D Biol. Crystallogr.*  
25 *60*, 2256-2268.
- 26  
27 [77] Dunwell, J. M., Purvis, A., Khuri, S. (2004) Cupins: the most functionally diverse protein  
28 superfamily? *Phytochemistry* 65, 7-17.
- 29 [78] Ma, J. C., Dougherty, D. A. (1997) The cation-pi interaction. *Chem. Rev.* 97, 1303-1324.
- 30 [79] Xing, G., Hoffart, L. M., Diao, Y., Prabhu, K. S., Amer, R. J., Reddy, C. C., Krebs, C.,  
31 Bollinger, J. M., Jr. (2006) A coupled dinuclear iron cluster that is perturbed by substrate  
32 binding in *myo*-inositol oxygenase. *Biochemistry* 45, 5393-5401.
- 33 [80] Doi, K., McCracken, J., Peisach, J., Aisen, P. (1988) The binding of molybdate to  
34 uteroferrin. Hyperfine interactions of the binuclear center with  $^{95}\text{Mo}$ ,  $^1\text{H}$ , and  $^2\text{H}$ . *J.*  
35 *Biol. Chem.* 263, 5757-5763.
- 36  
37 [81] Hirao, H., Morokuma, K. (2009) Insights into the (superoxo)Fe(III)Fe(III) intermediate and  
38 reaction mechanism of *myo*-inositol oxygenase: DFT and ONIOM(DFT:MM) study. *J.*  
39 *Am. Chem. Soc.* 131, 17206-17214.
- 40 [82] Zhou, J., Kelly, W. L., Bachmann, B. O., Gunsior, M., Townsend, C. A., Solomon, E. I.  
41 (2001) Spectroscopic studies of substrate interactions with clavaminase synthase 2, a  
42 multifunctional alpha-KG-dependent non-heme iron enzyme: Correlation with  
43 mechanisms and reactivities. *J. Am. Chem. Soc.* 123, 7388-7398.
- 44 [83] Neidig, M. L., Brown, C. D., Light, K. M., Fujimori, D. G., Nolan, E. M., Price, J. C., Barr,  
45 E. W., Bollinger, J. M., Jr., Krebs, C., Walsh, C. T., Solomon, E. I. (2007) CD and MCD  
46 of CytC3 and taurine dioxygenase: Role of the facial triad in alpha-KG-dependent  
47 oxygenases. *J. Am. Chem. Soc.* 129, 14224-14231.
- 48 [84] Rydzik, A. M., Brem, J., Struwe, W. B., Kochan, G. T., Benesch, J. L., Schofield, C. J.  
49 (2014) Ejection of structural zinc leads to inhibition of gamma-butyrobetaine  
50 hydroxylase. *Bioorg. Med. Chem. Lett.* 24, 4954-4957.
- 51 [85] Kamps, J. J., Khan, A., Choi, H., Lesniak, R. K., Brem, J., Rydzik, A. M., McDonough, M.  
52 A., Schofield, C. J., Claridge, T. D., Mecinovic, J. (2016) Cation-pi interactions  
53  
54  
55  
56  
57  
58  
59  
60

- 1  
2  
3 contribute to substrate recognition in gamma-butyrobetaine hydroxylase catalysis.  
4 *Chemistry* 22, 1270-1276.
- 5 [86] Mecozzi, S., West, A. P., Dougherty, D. A. (1996) Cation-pi interactions in aromatics of  
6 biological and medicinal interest: Electrostatic potential surfaces as a useful qualitative  
7 guide. *Proc. Natl. Acad. Sci. USA* 93, 10566-10571.
- 8 [87] Mecozzi, S., West, A. P., Dougherty, D. A. (1996) Cation-pi interactions in simple  
9 aromatics: Electrostatics provide a predictive tool. *J. Am. Chem. Soc.* 118, 2307-2308.
- 10 [88] Taverna, S. D., Li, H., Ruthenburg, A. J., Allis, C. D., Patel, D. J. (2007) How chromatin-  
11 binding modules interpret histone modifications: lessons from professional pocket  
12 pickers. *Nat. Struct. Mol. Biol.* 14, 1025-1040.
- 13 [89] Kamps, J. J., Huang, J., Poater, J., Xu, C., Pieters, B. J., Dong, A., Min, J., Sherman, W.,  
14 Beuming, T., Matthias Bickelhaupt, F., Li, H., Mecinovic, J. (2015) Chemical basis for  
15 the recognition of trimethyllysine by epigenetic reader proteins. *Nat. Commun.* 6, 8911.
- 16 [90] Agarwal, V., Peck, S. C., Chen, J. H., Borisova, S. A., Chekan, J. R., van der Donk, W. A.,  
17 Nair, S. K. (2014) Structure and function of phosphonoacetaldehyde dehydrogenase: The  
18 missing link in phosphonoacetate formation. *Chem. Biol.* 21, 125-135.
- 19 [91] Lee, J. H., Bae, B., Kuemin, M., Circello, B. T., Metcalf, W. W., Nair, S. K., van der Donk,  
20 W. A. (2010) Characterization and structure of DhplI, a phosphonate O-methyltransferase  
21 involved in dehydrophos biosynthesis. *Proc. Natl. Acad. Sci. U. S. A.* 107, 17557-17562.
- 22 [92] Chen, C. C. H., Zhang, H., Kim, A. D., Howard, A., Sheldrick, G. M., Mariano-Dunaway,  
23 D., Herzberg, O. (2002) Degradation pathway of the phosphonate ciliatine: Crystal  
24 structure of 2-aminoethylphosphonate transaminase. *Biochemistry* 41, 13162-13169.
- 25 [93] Yun, D., Dey, M., Higgins, L. J., Yan, F., Liu, H. W., Drennan, C. L. (2011) Structural basis  
26 of regioselectivity of a mononuclear iron enzyme in antibiotic fosfomycin biosynthesis.  
27 *J. Am. Chem. Soc.* 133, 11262-11269.
- 28 [94] Fox, B. G., Hendrich, M. P., Surerus, K. K., Andersson, K. K., Froland, W. A., Lipscomb, J.  
29 D., Münck, E. (1993) Mössbauer, EPR, and ENDOR studies of the hydroxylase and  
30 reductase components of methane monooxygenase from *Methylosinus trichosporium*  
31 Ob3b. *J. Am. Chem. Soc.* 115, 3688-3701.
- 32 [95] Woodland, M. P., Patil, D. S., Cammack, R., Dalton, H. (1986) Electron-spin-resonance  
33 studies of protein-A of the soluble methane monooxygenase from *Methylococcus*  
34 *capsulatus* (Bath). *Biochim. Biophys. Acta.* 873, 237-242.
- 35 [96] Fox, B. G., Surerus, K. K., Münck, E., Lipscomb, J. D. (1988) Evidence for a  $\mu$ -oxo-bridged  
36 binuclear iron cluster in the hydroxylase component of methane monooxygenase -  
37 Mössbauer and electron-paramagnetic-resonance studies. *J Biol. Chem.* 263, 10553-  
38 10556.
- 39 [97] Han, J. Y., Swarts, J. C., Sykes, A. G. (1996) Kinetic studies on the hydrazine and  
40 phenylhydrazine reductions of the *Escherichia coli* R2 subunit of ribonucleotide  
41 reductase. *Inorg. Chem.* 35, 4629-4634.
- 42 [98] Davydov, R., Kuprin, S., Gräslund, A., Ehrenberg, A. (1994) Electron-paramagnetic-  
43 resonance study of the mixed-valent diiron center in *Escherichia coli* ribonucleotide  
44 reductase produced by reduction of radical-free protein-R2 at 77-K. *J. Am. Chem. Soc.*  
45 116, 11120-11128.
- 46 [99] Davydov, R., Sahlin, M., Kuprin, S., Gräslund, A., Ehrenberg, A. (1996) Effect of the  
47 tyrosyl radical on the reduction and structure of the *Escherichia coli* ribonucleotide  
48 reductase. *J. Am. Chem. Soc.* 118, 11120-11128.
- 49  
50  
51  
52  
53  
54  
55  
56  
57  
58  
59  
60

- 1  
2  
3 reductase protein R2 diferric site as probed by EPR on the mixed-valent state.  
4 *Biochemistry* 35, 5571-5576.
- 5 [100] Davydov, R. M., Davydov, A., Ingemarson, R., Thelander, L., Ehrenberg, A., Gräslund, A.  
6 (1997) EPR study of the mixed-valent diiron sites in mouse and herpes simplex virus  
7 ribonucleotide reductases. Effect of the tyrosyl radical on structure and reactivity of the  
8 diferric center. *Biochemistry* 36, 9093-9100.
- 9 [101] Davydov, R. M., Menage, S., Fontecave, M., Gräslund, A., Ehrenberg, A. (1997) Mixed-  
10 valent  $\mu$ -oxo-bridged diiron complexes produced by radiolytic reduction at 77 K studied  
11 by EPR. *J. Biol. Inorg. Chem.* 2, 242-255.
- 12 [102] Atta, M., Andersson, K. K., Ingemarson, R., Thelander, L., Gräslund, A. (1994) EPR  
13 studies of mixed-valent Fe(III)-Fe(II) clusters formed in the R2 subunit of ribonucleotide  
14 reductase from mouse or herpes-simplex virus - mild chemical reduction of the diferric  
15 centers. *J. Am. Chem. Soc.* 116, 6429-6430.
- 16 [103] Horowitz, S., Trievel, R. C. (2012) Carbon-oxygen hydrogen bonding in biological  
17 structure and function. *J. Biol. Chem.* 287, 41576-41582.
- 18 [104] Adhikari, U., Scheiner, S. (2013) Magnitude and mechanism of charge enhancement of  
19 CH..O hydrogen bonds. *J. Phys. Chem. A* 117, 10551-10562.
- 20 [105] Bodea, S., Funk, M. A., Balskus, E. P., Drennan, C. L. (2016) Molecular basis of C-N  
21 bond cleavage by the glycol radical enzyme choline trimethylamine-lyase. *Cell Chem.*  
22 *Biol.* 23, 1206-1216.
- 23 [106] Horowitz, S., Dirk, L. M., Yesselman, J. D., Nimtz, J. S., Adhikari, U., Mehl, R. A.,  
24 Scheiner, S., Houtz, R. L., Al-Hashimi, H. M., Trievel, R. C. (2013) Conservation and  
25 functional importance of carbon-oxygen hydrogen bonding in AdoMet-dependent  
26 methyltransferases. *J. Am. Chem. Soc.* 135, 15536-15548.
- 27 [107] Starbird, C. A., Perry, N. A., Chen, Q., Berndt, S., Yamakawa, I., Loukachevitch, L. V.,  
28 Limbrick, E. M., Bachmann, B. O., Iverson, T. M., McCulloch, K. M. (2018) The  
29 structure of the bifunctional everninomicin biosynthetic enzyme EvdMO1 suggests  
30 independent activity of the fused methyltransferase-oxidase domains. *Biochemistry* 57,  
31 6827-6837.
- 32 [108] Marcotte, E. M., Pellegrini, M., H.-L., N., Rice, D. W., Yeates, T. O., Eisenberg, D. (1999)  
33 Detecting protein function and protein-protein interactions from genome sequences.  
34 *Science* 285, 751-753.
- 35 [109] Maddocks, S. E., Oyston, P. C. (2008) Structure and function of the LysR-type  
36 transcriptional regulator (LTTR) family proteins. *Microbiology* 154, 3609-3623.
- 37 [110] Kulakova, A. N., Kulakov, L. A., McGrath, J. W., Quinn, J. P. (2009) The construction of  
38 a whole-cell biosensor for phosphonoacetate, based on the LysR-like transcriptional  
39 regulator PhnR from *Pseudomonas fluorescens* 23F. *Microb. Biotechnol.* 2, 234-240.
- 40 [111] Kulakova, A. N., Kulakov, L. A., Villarreal-Chiu, J. F., Gilbert, J. A., McGrath, J. W.,  
41 Quinn, J. P. (2009) Expression of the phosphonoalanine-degradative gene cluster from  
42 *Variovorax sp* Pal2 is induced by growth on phosphonoalanine and phosphonopyruvate.  
43 *FEMS Microbiol. Lett.* 292, 100-106.
- 44 [112] Kulakova, A. N., Wisdom, G. B., Kulakov, L. A., Quinn, J. P. (2003) The purification and  
45 characterization of phosphonopyruvate hydrolase, a novel carbon-phosphorus bond  
46 cleavage enzyme from *Variovorax sp* Pal2. *J. Biol. Chem.* 278, 23426-23431.
- 47 [113] Mukhamedova, K. S., Glushenkova, A. I. (2000) Natural phosphonolipids. *Chem. Nat.*  
48 *Compd.* 36, 329-341.
- 49  
50  
51  
52  
53  
54  
55  
56  
57  
58  
59  
60

- 1  
2  
3 [114] Kirkpatrick, D. S., Bishop, S. H. (1973) Phosphonoprotein - Characterization of  
4 aminophosphonic acid rich glycoproteins from sea anemones. *Biochemistry* 12, 2829-  
5 2840.  
6  
7 [115] Hilderbrand, R. L., Joseph, J. L., Lubansky, H. J., Henderson, T. O. (1977) Biology of  
8 Alkylphosphonic Acids, Naval Health Research Center, San Diego, CA.  
9 [116] Kittredge, J. S., Isbell, A. F., Hughes, R. R. (1967) Isolation and characterization of N-  
10 methyl derivatives of 2-aminoethylphosphonic acid from sea anemone *Anthopleura*  
11 *xanthogrammica*. *Biochemistry* 6, 289-295.  
12 [117] Kittredge, J. S., Roberts, E. (1969) A carbon-phosphorus bond in nature. *Science* 164, 37-  
13 42.  
14 [118] Kataoka, H., Sakiyama, N., Makita, M. (1989) Determination of 2-aminoethylphosphonic  
15 acid and its N-methyl derivative in animal-tissues by gas-chromatography with flame  
16 photometric detection. *Agr. Biol. Chem.* 53, 2791-2796.  
17 [119] McGrath, J. W., Chin, J. P., Quinn, J. P. (2013) Organophosphonates revealed: new  
18 insights into the microbial metabolism of ancient molecules. *Nat. Rev. Microbiol.* 11,  
19 412-419.  
20 [120] Quinn, J. P., Kulakova, A. N., Cooley, N. A., McGrath, J. W. (2007) New ways to break  
21 an old bond: the bacterial carbon-phosphorus hydrolases and their role in biogeochemical  
22 phosphorus cycling. *Environ. Microbiol.* 9, 2392-2400.  
23 [121] Villarreal-Chiu, J. F., Quinn, J. P., McGrath, J. W. (2012) The genes and enzymes of  
24 phosphonate metabolism by bacteria, and their distribution in the marine environment.  
25 *Front Microbiol* 3, 19.  
26 [122] Peck, S. C., van der Donk, W. A. (2013) Phosphonate biosynthesis and catabolism: a  
27 treasure trove of unusual enzymology. *Curr. Opin. Chem. Biol.* 17, 580-588.  
28 [123] Kononova, S. V., Nesmeyanova, M. A. (2002) Phosphonates and their degradation by  
29 microorganisms. *Biochemistry-Moscow* 67, 184-195.  
30 [124] Mus, F., Crook, M. B., Garcia, K., Garcia Costas, A., Geddes, B. A., Kouri, E. D.,  
31 Paramasivan, P., Ryu, M. H., Oldroyd, G. E., Poole, P. S., Udvardi, M. K., Voigt, C. A.,  
32 Ane, J. M., Peters, J. W. (2016) Symbiotic nitrogen fixation and the challenges to its  
33 extension to nonlegumes. *Appl. Environ. Microbiol.* 82, 3698-3710.  
34 [125] Bardin, S., Dan, S., Osteras, M., Finan, T. M. (1996) A phosphate transport system is  
35 required for symbiotic nitrogen fixation by *Rhizobium meliloti*. *J. Bacteriol.* 178, 4540-  
36 4547.  
37 [126] Eckardt, N. A. (2005) Insights into plant cellular mechanisms: Of phosphate transporters  
38 and arbuscular mycorrhizal infection. *Plant Cell* 17, 3213-3216.  
39 [127] Tang, C., Hinsinger, P., Drevon, J. J., Jaillard, B. (2001) Phosphorus deficiency impairs  
40 early nodule functioning and enhances proton release in roots of *Medicago truncatula* L.  
41 *Ann. Bot.* 88, 131-138.  
42 [128] Høgh-Jensen, H., Schjoerring, J. K., Soussana, J. F. (2002) The influence of phosphorus  
43 deficiency on growth and nitrogen fixation of white clover plants. *Ann. Bot.* 90, 745-753.  
44 [129] King, G. M. (1988) *Distributions and metabolism of quaternary amines in marine*  
45 *sediments.*, Blackburn, T. H., and Sørensen, J. , Ed., John Wiley & Sons, New York, NY,  
46 USA.  
47 [130] Bernard, T., Pocard, J. A., Perroud, B., Lerudulier, D. (1986) Variations in the response of  
48 salt-stressed *Rhizobium* strains to betaines. *Arch. Microbiol.* 143, 359-364.  
49  
50  
51  
52  
53  
54  
55  
56  
57  
58  
59  
60

- 1  
2  
3 [131] Lerudulier, D., Bernard, T. (1986) Salt tolerance in *Rhizobium* - a possible role for  
4 betaines. *FEMS Microbiol. Lett.* 39, 67-72.  
5 [132] Lerudulier, D., Bernard, T., Goas, G., Hamelin, J. (1984) Osmoregulation in *Klebsiella*  
6 *pneumoniae* - Enhancement of anaerobic growth and nitrogen-fixation under stress by  
7 proline betaine, gamma-butyrobetaine, and other related compounds. *Can. J. Microbiol.*  
8 30, 299-305.  
9 [133] Boncompagni, E., Osteras, M., Poggi, M. C., Le Rudulier, D. (1999) Occurrence of choline  
10 and glycine betaine uptake and metabolism in the family *Rhizobiaceae* and their roles in  
11 osmoprotection. *Appl. Environ. Microbiol.* 65, 2072-2077.  
12 [134] Goldmann, A., Boivin, C., Fleury, V., Message, B., Lecoecur, L., Maille, M., Tepfer, D.  
13 (1991) Betaine use by rhizosphere bacteria - Genes essential for trigonelline, stachydrine,  
14 and carnitine catabolism in *Rhizobium meliloti* are located on Psym in the symbiotic  
15 Region. *Mol. Plant Microbe* 4, 571-578.  
16 [135] Ticak, T., Kountz, D. J., Girosky, K. E., Krzycki, J. A., Ferguson, D. J. (2014) A  
17 nonpyrrolysine member of the widely distributed trimethylamine methyltransferase  
18 family is a glycine betaine methyltransferase. *Proc. Natl. Acad. Sci. U S A* 111, E4668-  
19 4676.  
20  
21  
22  
23  
24  
25

## 26 For Table of Contents Use Only

27  
28 Title: A new microbial pathway for organophosphonate degradation catalyzed by two previously  
29 misannotated non-heme-iron oxygenases  
30  
31

32  
33 Authors: Lauren J. Rajakovich, Maria-Eirini Pandelia, Andrew J. Mitchell, Wei-chen Chang, Bo  
34  
35 Zhang, Amie K. Boal, Carsten Krebs, J. Martin Bollinger, Jr.  
36

